Analysis of multiple programmed cell death-related prognostic genes and functional validations of necroptosis-associated genes in oesophageal squamous cell carcinoma

Kui Cao,[a,h] Jinhong Zhu,[b,c,h] Mengdi Lu,[a] Jinfeng Zhang,[a] Yingnan Yang,[a] Xiaodong Ling,[a] Luquan Zhang,[a] Cuicui Qi,[a] Shenshui Wei,[b] Yanqiao Zhang,[d,e,f,g,**] and Jianqun Ma[a,*]

[a]Department of Thoracic Surgery, Harbin Medical University Cancer Hospital, 150 Haping Road, Harbin, 150040, Heilongjiang, China
[b]Biobank, Harbin Medical University Cancer Hospital, 150 Haping Road, Harbin, 150040, Heilongjiang, China
[c]Department of Clinical Laboratory, Harbin Medical University Cancer Hospital, 150 Haping Road, Harbin, 150040, Heilongjiang, China
[d]Department of Gastrointestinal Medical Oncology, Harbin Medical University Cancer Hospital, 150 Haping Road, Harbin, 150040, Heilongjiang, China
[e]Clinical Research Center for Colorectal Cancer in Heilongjiang, Harbin, China
[f]Key Laboratories of Tumor Immunology in Heilongjiang, Harbin, China
[g]Translational Medicine Research and Cooperation Center of Northern China, Heilongjiang Academy of Medical Sciences, Harbin, China

eBioMedicine
2024;99: 104920
Published Online xxx
https://doi.org/10.1016/j.ebiom.2023.104920

Summary

Background Oesophageal squamous cell carcinoma (ESCC) is a lethal malignancy. Immune checkpoint inhibitors (ICIs) showed great clinical benefits for patients with ESCC. We aimed to construct a model predicting prognosis and response to ICIs by integrating diverse programmed cell death (PCD) forms.

Methods Genes related to 14 PCDs were collected to generate multi-gene signatures, including apoptosis, necroptosis, pyroptosis, ferroptosis, and cuproptosis. Bulk and single-cell RNA transcriptome datasets were used to develop and validate the model. We assessed the functions of two necroptosis-related genes in ESCC cells by Western blot, co-immunoprecipitation (Co-IP), LDH release assay, CCK-8, and migration assay, followed by immunohistochemistry (IHC) staining on samples of patients with ESCC (n = 67).

Findings We built and validated a 16-gene prognostic combined cell death index (CCDI) by combining immunogenic cell death (ICD) and necroptosis signatures. The CCDI could also predict response to ICIs in cancer, as shown by Tumour Immune Dysfunction and Exclusion (TIDE) analysis, confirmed in four independent ICI clinical trials. Trajectory analysis revealed that HOOK1 and CUL4A might affect ESCC cell fate. We found that HOOK1 induced necroptosis and inhibited the proliferation and migration of ESCC cells, while CUL4A exhibited the opposite effects. Co-IP assay confirmed that HOOK1 and CUL4A promoted and reduced necrosome formation in ESCC cells. Data from patients with ESCC further supported that HOOK1 and CUL4A might be a tumour suppressor and oncogene, respectively.

Interpretation We constructed a CCDI model with potential in predicting prognosis and response to ICIs in cancer. HOOK1 and CUL4A in the CCDI model are crucial prognostic biomarkers in ESCC.

Funding The Natural Science Foundation of China [82172786], The National Cancer Center Climbing Fund of China [NCC201908B06], The Natural Science Foundation of Heilongjiang Province [LH2021H077].

Keywords: Programmed cell death; Single-cell RNA-Seq; ESCC; Immune checkpoint inhibitor

*Corresponding author.
**Corresponding author. Department of Gastrointestinal Medical Oncology, Harbin Medical University Cancer Hospital, 150 Haping Road, Harbin, 150040, Heilongjiang, China.
E-mail addresses: jianqunma@hrbmu.edu.cn (J. Ma), yanqiaozhang@ems.hrbmu.edu.cn (Y. Zhang).
[h]These authors equally contributed to the manuscript.

Research in context

Evidence before this study

Oesophageal squamous cell carcinoma (ESCC) is a common and lethal malignancy with an unsatisfactory prognosis. Immune checkpoint inhibitors (ICIs) have shown promising and durable therapeutic effects on some patients with ESCC. Therefore, patient classification accuracy urgently needs to be enhanced regarding prognosis and response to ICIs. Molecular biomarkers predicting cancer progression, prognosis, and therapy sensitivity have been used to improve cancer treatment. However, current single biomarkers may not characterise tumour subtypes well due to the molecular heterogeneity of cancer. The recent breakthrough of unbiased high-throughput sequencing (seq) techniques and advances in deep machine learning algorithms analysing big data have revolutionised the understanding of cancer biology. As a result, over the past few years, numerous predictive multi-gene models were generated using sequencing data to predict clinical outcomes and responses to anti-cancer therapies, including chemotherapy, targeted therapy, and immunotherapy. Among them, predictive models based on different programmed cell death (PCD) are noteworthy due to their importance in tumour development, regression, and prognosis. However, most of such models were developed upon single PCD forms. Predictive models derived from all known PCD types might better represent tumour characteristics and thereby be more robust predictive biomarkers in clinical practice than those developed from single types of cell death. The study had several aims: 1) to build a multi-gene signature predictive of prognosis and response to ICIs, 2) to conduct trajectory analysis to identify essential genes in the predictive signature using published single-cell RNA-seq (scRNA-seq) data, and 3) to validate functions of the selected genes.

Added value of this study

First, this study yielded and validated a combined cell death index (CCDI) comprising 16 genes selected from the ICD and necroptosis signatures. Second, the CCDI may serve as a biomarker to predict response to ICIs, as suggested by TIDE analysis and validations in four independent ICI clinical trials of different cancers. Third, we used public scRNA-seq data to identify two essential genes (HOOK1 and CUL4A) that might impact ESCC cell fate. Finally, *in vitro* studies demonstrated that HOOK1 overexpression activated the formation of necrosomes and impaired the proliferation and migration of ESCC cells. Parallel studies showed the opposite effects of CUL4A on ESCC cells. Clinical sample analyses supported that HOOK1 and CUL4A were tumour-suppressing and -promoting genes, respectively.

Implications of all the available evidence

We constructed a CCDI model predicting prognosis and response to ICIs in cancer. Furthermore, bioinformatic and functional evidence confirmed that HOOK1 and CUL4A in the CCDI model may have crucial regulatory roles in ESCC and are potential therapeutic targets and prognostic biomarkers in ESCC.

Introduction

Oesophageal cancer is the seventh most common cancer worldwide, including squamous cell carcinoma and adenocarcinoma.[1] Oesophageal squamous cell carcinoma (ESCC) is more prevalent in China, accounting for 90% of cases.[1] Surgery is the primary treatment for patients with ESCC. However, treatment options are very limited for patients with advanced or metastatic ESCC, for whom the mainstay first-line therapy has been restricted to platinum plus paclitaxel/fluorouracil chemotherapy over the past few decades with an unsatisfactory median overall survival (OS) of less than 12 months.[2] Recently, anti-programmed death 1 (PD-1) therapy has shown great promise in ESCC treatment, especially in combination with chemotherapy in neoadjuvant and first-line settings.[2] However, it remains demanding to identify the subpopulation of patients with ESCC suitable for immune checkpoint inhibitors (ICIs).[3] Therefore, it is urgent to develop robust models predictive of the prognosis and immunotherapy response to individualise clinical treatment.

Programmed cell death (PCD), also known as regulated cell death, does not occur accidentally but is precisely orchestrated by various mechanisms. Based on triggering stresses, morphological features, regulatory signalling pathways, and effector molecules, PCD is categorised into apoptosis (intrinsic and extrinsic), entotic cell death, necroptosis, cuproptosis, oxeiptosis, ferroptosis, alkaliptosis, pyroptosis, parthanatos, autophagy-dependent cell death, lysosome-dependent cell death, and netotic cell death.[4] Briefly, intrinsic apoptosis is triggered by damaged mitochondria and mediated by caspase 3 (CASP3), CASP6, and CASP7. On the contrary, extrinsic apoptosis requires ligand-membrane receptor interactions and is generally mediated by death receptors (e.g., fas cell surface death receptor and TNF receptor superfamily member 1A), relying on the activity of initiator caspases, CASP8 and CASP10.[4] Entotic cell death (Entosis) is referred to as cell cannibalism. One example is that healthy cells may engulf and kill nearby cancer cells.[5] Necroptosis is characterised by the formation of necrosomes consisting of receptor-interacting protein kinase 1 (RIPK1) and RIPK3, and mixed lineage kinase domain-like pseudokinase (MLKL) phosphorylation.[6] Cuproptosis is a type of copper-induced cell death characterised by lipoylation

of the TCA cycle protein.[7] Both alkaliptosis[8] and oxeiptosis[9] were discovered in 2018. The former is caused by intracellular alkalinisation,[8] and the latter is initiated by oxygen radical activated KEAP1-PGAM5-AIFM1 pathway, independent of caspases.[9] Ferroptosis is caused by iron overload and the ensuing lethal peroxidised lipids accumulation, which can be antagonised by glutathione peroxidase 4 (GPX4) GPX4 and glutathione (GSH).[10] Pyroptosis often involves the activation of the inflammasome, in which the essential event is the cleavage of the gasdermin (GSDM) superfamily by caspase-1, 3, 4, or 5 and the formation of pores with the N terminal of GSMDs in the plasma membrane.[11] Parthanatos is an oxidative stress-triggered and poly [ADP-Ribose] Polymerase 1 (PARP1) dependent PCD with DNA damage and chromatolysis.[12] Autophagy is related to the formation of autophagosome containing cytosolic components and damaged organelles, which can either promote cell survival or induce cell death in a different context.[13] Lysosome-dependent cell death is induced by increased lysosomal membrane permeabilization, which further leads to the leakage of hydrolytic enzymes into the cytosol.[14] Netotic cell death is driven by the formation and release of neutrophil extracellular traps (NETs) by leukocytes (neutrophils, mast cells, eosinophils, and basophils), epithelial cells, and cancer cells upon infection or injury.[15] PCD is also classified into immunogenic cell death (ICD), tolerogenic cell death (TCD), and silent cell death. ICD triggers immune responses and plays a crucial role in the development and metastasis of malignant tumours.[4,16] Over the past years, tremendous efforts have been made to develop predictive models with signature genes of single PCD forms, and moderate predictive accuracy is achieved in predicting cancer prognosis and drug resistance.[17–23] However, considerable redundancy and crosstalk have been observed among the signalling pathways regulating diverse cell death forms. Therefore, it is reasonable to speculate that a predictive model based on all known PCD types should better represent tumour characteristics than single types of cell death. In this study, we collected the signature genes of 13 PCD forms and the representative genes of ICD to establish various prognostic models and compare their predictive abilities. ICD was analysed because of its critical implication in tumour immunity. Consequently, we generated an optimal model of 16 genes by integrating necroptosis and ICD, called combined cell death index (CCDI), using gene expression datasets from bulk tumours.

Cancer cell death is fundamental in reshaping the tumour immune microenvironment (TIME).[24] For example, tumour cell debris serves as antigens, which can be captured, processed, and presented by conventional dendritic cells (cDCs). Some types of cell death with cellular membrane disruption release damage-associated molecular patterns (DAMPs) and inflammatory cytokines, such as necroptosis and pyroptosis.[16] In contrast, some studies show that cell death can also be immunosuppressive, both directly and indirectly, via the recruitment of myeloid cells, such as immunosuppressive macrophage subsets.[25] Given the tight linkage between TIME and immunotherapy response, it has been a research hot spot to identify and induce immunogenic forms of cell death to optimise the immune response against cancer, especially in the era of ICIs. Moreover, accumulating evidence indicates that patients with cancer having different prognoses frequently show differences in tumour immune microenvironments and response to ICIs. Many prognostic signatures could predict sensitivity of patients with cancer to chemotherapy and immunotherapy to some content.[26–29] Therefore, we further evaluated the CCDI's discriminating accuracy in predicting immunotherapy responses and validated its predictive value in four ICI clinical trials.[30–33]

Bulk technologies have long contributed to cancer research and translational medicine. However, this methodology could only detect merged signals from heterogeneous cell groups, including tumour cells, fibroblasts, endothelial cells, and different infiltrating immune subsets. Such information could merely reflect the molecular states and functions of the dominant cell populations. As a result, the critical roles of less abundant cell populations in tumour development have often been neglected. The striking advances in single-cell sequencing technology enable widespread application of the single-cell analysis in cancer research to accurately delineate each cellular composition in the tumour microenvironment (TME) and further dissect activities of signalling pathways in a cell type wise.[34–36] Furthermore, the ensuing machine-learning single-cell algorithms allow us to analyse and visualise cell-to-cell interactions.[37] Therefore, we further investigated the role of CCDI genes in the single-cell resolution, followed by *in vitro* functional analyses and validation in the in-house ESCC samples.

Methods

Data source

RNA-sequencing (RNA-seq) data and clinical data of patients were downloaded from the Gene Expression Omnibus (GEO) (https://www.ncbi.nlm.nih.gov/geo) and The Cancer Genome Atlas (TCGA) (https://www.cancer.gov/tcga/). This study involves eight published datasets, including TCGA-ESCC (n = 81), GSE53625 (n = 358), GSE53624 (n = 238), GSE78220 (n = 28), GSE67501 (n = 11), GSE165252 (n = 77), GSE196756 (n = 6), GSE188900 (n = 7), and the IMvigor210 cohort (n = 310). The IMvigor210 cohort was retrieved from previously published literature.[30] For genes detected by multiple probes, the average expression levels were used. They were quantile normalised by log scale transformation to ensure normalisation.

We used GSE53625 as the training set and the TCGA-ESCC and GSE53624 as the validation set for the prognostic model of ESCC. We used two ESCC scRNA-seq datasets, GSE196756 (3 normal vs 3 tumour tissues) and GSE188900 (1 normal vs 6 tumour tissues), to assess the dynamic changes of the CCDI-related genes during the evolution of different cells in the TME. We also analysed the interactions among ESCC, immune, and stromal cells. Moreover, data from four ICI clinical trials were used to assess the predictive ability of the CCDI model for immunotherapy sensitivity, including patients with metastatic urothelial carcinoma undergoing anti-PD-L1 therapy (the IMvigor210 cohort), patients with melanoma treated with anti-PD-1 therapy (GSE78220), patients with renal cell carcinoma receiving anti-PD-1 treatment (GSE67501) and patients with oesophageal adenocarcinoma (EAC) treated with anti-PD-L1 therapy (GSE165252).

The gene sets associated with the different forms of PCD were collected from published literature and databases, including intrinsic apoptosis (n = 500), extrinsic apoptosis (n = 500), entotic cell death (n = 23), necroptosis (n = 500), cuproptosis (n = 17), oxeiptosis (n = 146), ferroptosis (n = 283), alkaliptosis (n = 73), pyroptosis (n = 387), parthanatos (n = 23), autophagy-dependent cell death (n = 232), lysosome-dependent cell death (n = 194), netotic cell death (n = 11) and immunogenic cell death (ICD) (n = 500).[4,38–42]

Construction and validation of the CCDI model

The GSE53625 dataset was used as the training set to construct and compare the prognostic models of 14 cell death forms and the CCDI model. The TCGA-ESCC and GSE53624 datasets were used as external validation sets to verify the predictive power of necroptosis, CDI, and CCDI models. Firstly, univariable Cox analysis regarding overall survival (OS) was performed to screen significant prognostic genes from all the signature genes of 14 cell death forms. Then, multivariable Cox regression analysis was performed to construct prognostic models for each form of cell death based on the coefficients of genes. The multivariable Cox regression model was applied to select variables through the "bidirectional" stepwise selection that includes backward stepwise elimination and forward stepwise selection, while the Akaike information criterion (AIC) but not *P*-values was used as a variable selection criterion. This analysis was implemented with the "stepAIC" function in package "MASS".[43] When using AIC to select variables for a multivariable model, the alpha level is not explicitly set as in traditional hypothesis testing, but rather a lower AIC value that indicates a better model fit. The AIC considers the statistical fit degree of the model and the number of independent variables used for fitting. The model with a smaller AIC value is preferred, which indicates that the model obtains a sufficient fit degree with fewer independent variables.[44]

Time-dependent receiver operating characteristic (ROC) and ROC were created. The area under the curve (AUC) was used to evaluate the efficiency of each prognostic model. We obtained seven prognostic models with AUC > 0.7 for 1, 2, 3, 4, and 5 years. To minimise the uncertainty in the AUC estimate, we removed three models (pyroptosis, lysosome-dependent cell death and extrinsic apoptosis) with a lower 95% confidence limit smaller than 0.7 for 1-year AUC. Subsequently, we employed logistic regression to recreate a series of combined models comprising 2–4 independent prognostic signatures. Among them, CCDI, the integrated model incorporating necroptosis and ICD, had the largest AUC and was selected for the rest of the study. Each patient with ESCC in the dataset was assigned a risk score, that is, the CCDI risk score calculated from the following equation: CCDI/Risk score = $\frac{\exp(\beta_0+\beta_1\chi_{ICD}+\beta_2\chi_{necroptosis})}{1+\exp(\beta_0+\beta_1\chi_{ICD}+\beta_2\chi_{necroptosis})}$. β_0 is the constant term; β_1 and β_2 are the logistic regression coefficients, while χ_{ICD} and $\chi_{\text{necroptosis}}$ are risk scores computed from "Risk score $_{\text{ICD}} = \sum_{i=1}^{n}\beta_i x_i$" and "Risk score $_{\text{Necroptosis}} = \sum_{j=1}^{n}\beta_j x_j$", respectively. Patients were divided into two groups regarding a cutoff value of CCDI score determined using the minimum *P* value method in the Kaplan–Meier curve. Patients with a risk score higher than this cutoff value were considered high risk, while the rest were deemed low risk. The distribution differences of high- and low-risk groups were explored by the "umap" R packages. To internally validate the 14 individual PCD models and the CCDI in the training set, we created 1000 bootstrap datasets of the same size (n = 179) by sampling with replacement. The TCGA-ESCC (n = 81) and GSE53624 (n = 238) were used as the two independent external validation sets.

Estimation of the capacity of the CCDI model in predicting responses to ICIs

Tumour Immune Dysfunction and Exclusion (TIDE, http://tide.dfci.harvard.edu/) is a web tool developed to predict immune checkpoint blockade (ICB) response. This database was established by integrating large-scale omics data and biomarkers collected from 188 tumour cohorts, 12 published ICB trials, and eight CRISPR screens designed to discover modulators regulating lymphocyte-mediated cancer killing and the anti-cancer immune response.[17] Therefore, TIDE can be adopted to predict patients' response to ICBs by analysing the gene expression profile of the tumour. The threshold of the TIDE score was 0 by default, i.e., a patient with a TIDE <0 was defined as a responder of ICBs. Additionally, four independent immunotherapy trials (IMvigor210 dataset, GSE78220, GSE67501 and GSE165252) were used to detect differences in immunotherapy efficacy between high- and low-risk groups.[30–33] The immunotherapy approach produced four outcomes: complete response (CR), partial

response (PR), progressive disease (PD), and stable disease (SD).

Evaluation of immune cell infiltration

The differences in immune cell infiltration in high- and low-risk groups were assessed by the MCP-counter method[45] (cytotoxic lymphocytes, B cell lineage, CD8+ T cells, myeloid dendritic cells, NK cells, T cells, monocytic lineage cells, neutrophils, endothelial cells, and fibroblasts) and the CIBERSORT method (naive and memory B cells, plasma cells, NK cells, myeloid subsets, and 7 T cell types). In addition to this, the differences in immune cell infiltration between high- and low-risk groups were also explored using another five immune cell infiltration assessment methods (TIMER,[46] XCell,[47] EPIC,[48] QUANTISEQ,[49] CIBERSORT-ABS[50]) from the TIMER 2.0 website. The correlations between the risk score and the immune infiltrated cells were explored using Pearson correlation analysis. We also calculated immune scores for all subjects using the Estimation of STromal and Immune cells in Malignant Tumours using Expression data (ESTIMATE)-an algorithm that allows us to deduce the composition of stromal and immune cells in tumour samples using transcriptional profiles of cancer samples.[51] Single-sample gene set enrichment analysis (ssGSEA) based on the expression of 141 immune signature genes was carried out to compute immune scores to predict the level of infiltrating immune cells.

Pathways and function enrichment analysis

Gene set variation analysis (GSVA, "GSVA" R package) and Gene Set Enrichment Analysis (GSEA) software (version 4.0.1, http://www.gsea-msigdb.org/gsea/index.jsp) were used to compare high- and low-risk groups. The immunologic signature gene sets (C7), KEGG (C2), and Hallmark gene sets (H) were applied to dissect differential immune cell subsets, signalling pathways, biological states, and processes in the high- and low-risk groups. As the official literature of GSEA suggested, a false discovery rate (FDR) value of 0.25 was used as a cutpoint.[52] A GSEA result with $P < 0.05$ and FDR < 0.25 was considered statistically significant.[52]

Analysis of single-cell RNA-sequencing data

Single-cell data were analysed using the "Seurat", "SingleR", "Cellchat" and "Monocle2" R packages. First, the 10X data matrix was imported into Seurat V3.10 (https://satijalab.org/seurat) for data filtering, sample integration, gene normalisation, downscaling, and data visualisation. All samples were integrated into one object using Seurat's "IntegrateData" feature. To retain high-quality scRNA-seq data for the following analysis, three measures were applied to filter the raw data for each cell. Cells with low (<200) or high (>2500) feature counts and a high percentage of mitochondrial genes (>25%) were removed. The "RunHarmony" function of the "harmony" R package was employed to de-batch all samples. Dimensionality reduction was accomplished using Seurat's "RunPCA", "UMAP", and "TSNE" functions. Then, the top 40 principal components with the highest variance (resolution = 0.4) were used to visualise the clustering of single cells according to the clustering of cells.

For cluster annotation, we combined reference data from CellMarker (http://xteam.xbio.top/CellMarker/), SingleR, and published literature for cell annotation.[35,53,54] Cell–cell interactions and receptor–ligand pairs between the major cell types were probed using Cellchat V1.0.0 (http://www.cellchat.org/). Potential interactions between cell types were estimated by gene expression levels deduced from 1000 interchange assays. Regarding cellular evolutionary trajectories, the R package "Monocle2" was used to infer cellular trajectories using a gene-cell matrix at the UMI count scale extracted from the Seurat subset as the input data set after downscaling and cell sorting, using default parameters.[55]

Patients

We retrospectively recruited 67 patients with ESCC who underwent surgical treatment at the Harbin Medical University Cancer Hospital from March 2012 to December 2016.

Age, biological sex, and clinical information of patients were retrieved from electronic medical records in the hospital information system (Supplemental Table S1). Each patient was followed up for more than five years. The eligible patients met the following criteria: pathologically confirmed ESCC, complete prognostic follow-up information, no preoperative anticancer therapy, and no severe complications affecting prognosis in the perioperative period. Paraffin-embedded samples were collected for these patients. We also selected snap-frozen tumours and peri-tumoral tissues from an extra 12 patients with ESCC. The TNM classification of malignancy (TNM) for patients with ESCC was determined according to the guidelines of the American Joint Committee on Cancer (AJCC) and the International Union Against Cancer (UICC) (2017).

Cell culture and reagents

Oesophageal epithelial cells (HET-1A) (RRID: CVCL_3702) and ESCC cells (KYSE410, KYSE30, KYSE510, KYSE450, and KYSE150) (RRID: CVCL_1352, RRID: CVCL_1351, RRID: CVCL_1354, RRID: CVCL_1353 and RRID: CVCL_1348) were obtained from the Cell Bank of Chinese Academy of Sciences (Shanghai, China) and Procell Life Science&Technology Co., Ltd (Wuhan, China). Cell lines were cultured in RPMI 1640 medium (PM150110, Procell, China) with 10% fetal bovine serum (164210, Procell, Wuhan, China), penicillin G (100 U/ml, BYT-C0222, Beyotime, China), and streptomycin (100 μg/ml, BYT-C0222,

Beyotime, China) and maintained in a humidified incubator with 5% CO2, at 37 °C. All cell lines tested negative for mycoplasma throughout the study. The short tandem repeat (STR) profiling was used to verify the identity of each cell line. Cisplatin (HY-17394, MedChemExpress, Monmouth Junction, NJ, USA), necrostatin-1(Nec-1) (HY-15760, MedChemExpress, Monmouth Junction, NJ, USA), RIPA-56 (HY-101032, MedChemExpress, Monmouth Junction, NJ, USA) and necrosulfonamide (NSA) (HY-100573, MedChemExpress, Monmouth Junction, NJ, USA) were used to treat cells for 24 h to induce and inhibit necroptosis, respectively.

Plasmids and transfection

Plasmids overexpressing HOOK1, CUL4A, and empty vectors (CMV-enhancer-MCS-3FLAG-SV40-Puromycin) were purchased from Shanghai Genechem Co., Ltd. Cells in 6-well plates were transfected with empty vectors or plasmids encoding HOOK1 and CUL4A (plasmid 50 nM) using jetPRIME® transfection reagent (101000027, Polyplus Transfection Inc. New York, NY, USA) when reaching 80% confluency. Cells were kept in the medium for 24 h before being used for experiments.

Western blot analysis

The collected tissue was first well-ground using a homogeniser, lysed by adding RIPA lysis (P0013B, Beyotime, China) solution for 20 min, and then centrifuged at high speed (13,500 rpm for 15 min). Cell lysis was also prepared using the RIPA method. The protein samples were separated on SDS-PAGE (PG112, Epizyme Biotech, Shanghai, China) and transferred to PVDF membranes (ISEQ00010, Millipore, USA). The resulting blots were incubated with primary antibides against hook microtubule tethering protein 1 (HOOK1) (1:750, K003840P, Solarbio, Beijing, China), CUL4A (1:1000, K008800P, Solarbio, Beijing, China), MLKL (1:1000, Cat.#: 380559, Zen Biotechnology Co., Ltd, Chengdu, China), Phospho-MLKL (Ser358) (1:1250, Cat# 382136, Zen Biotechnology Co., Ltd, Chengdu, China), RIPK3 (1:1000, Cat# AF4808, RRID: AB_2844793, Affinity Biosciences, China), Phospho-RIPK3 (3:5000, Cat# 93654, RRID: AB_2800206, Cell Signaling Technology, China), RIPK1 (1:1000, Cat# 3493, RRID: AB_2305314, Cell Signaling Technology, China), GAPDH (1:2000, Cat# 60004-1-Ig, RRID: AB_2107436, Proteintech, Wuhan, China), and the secondary antibody (1:2000, Cat.# A212020, Abbkine, China; 1:2000, SA00001-1, Proteintech, China). For details, please refer to the previous publication.[56]

Co-immunoprecipitation (Co-IP)

Briefly, HOOK1-overexpressing KYSE150, CUL4A-overexpressing KYSE440 cells, or corresponding control cells were collected and lysated in IP lysis buffer with the addition of PMSF (protease inhibitor, ST505, Beyotime, China). All procedures were carefully executed on ice. The resulting supernatants were incubated with agarose-conjugated anti-RIPK1 antibody (Cat# 3493, RRID: AB_2305314, Cell Signaling Technology, China) or IgG (Cat# AC005, ABclonal, Wuhan, China) overnight at 4 °C. The immunoprecipitated beads were then washed three times, eluted with 1X loading buffer (P0015A, Beyotime, China), and boiled at 99 °C for 5 min. Upon the removal of beads, these samples were subjected to Western blot analysis and probed with the anti-RIPK1 (Cat# 3493, RRID: AB_2305314, Cell Signaling Technology, China), anti-RIPK3 (Cat# AF4808, RRID: AB_2844793, Affinity Biosciences, China), anti-MLKL (Cat.#: 380559, Zen Biotechnology Co., Ltd, Chengdu, China), or anti-GAPDH antibodies (Cat# 60004-1-Ig, RRID: AB_2107436, Proteintech, Wuhan, China).

Wound healing assay and migration assay

Cells are seeded in 6-well plates. Vertical scratches were generated on the monolayer when the cells reached 95% confluence. Afterwards, a serum-free medium was used to maintain the cells. Images were taken, and wound gaps were measured at 0 and 24 h. Migration assays were performed using Transwell chambers (8 μm; 3422, Corning, Tewksbury, MA, USA). A serum-free cell suspension was added to the upper wells of the chambers at a density of 3×10^4 cells/well, while the lower wells of the chambers contained 1640 (PM150110, Procell, China) supplemented with 10% FBS (164210, Procell, Wuhan, China) and then maintained in an incubator at 37 °C for 24 h. Migrating cells were fixed with 4% paraformaldehyde, stained with 0.1% crystal violet, and counted under a microscope.

Cell viability and LDH release assay

Cancer cell suspensions were added to 96-well plates at a density of 5000 cells/well. After attachment, cell viability was determined at 0, 24, 48, and 72 h using the Dojindo Cell Counting Kit-8 (CCK-8, GK10001, GlpBio, USA) according to the manufacturer's instructions. An appropriate number of ESCC cells were inoculated into 96-well cell culture plates such that the cell confluence at the time of the assay did not exceed 80–90%. LDH levels were measured using the Lactate Dehydrogenase Cytotoxicity Assay Kit (LDH Cytotoxicity Assay Kit, C0016, Beyotime, China).

Immunohistochemistry (IHC) staining

Paraffin-embedded samples were cut into 3–4 μm sections using a paraffin microtome (Leica, Germany) and mounted on poly-L-lysine-coated slides. Immunohistochemical analyses were performed using primary antibodies against HOOK1 (at 1:150 dilution, K110729P, Solarbio, Beijing, China) and cullin 4A (CUL4A) (at 1:100 dilution, K008800P, Solarbio, Beijing, China).

IHC staining was performed according to the standard protocol described elsewhere.[57] Each sample was designated as 1 (negative), 2 (weakly positive), and 3 (strongly positive) based on relative staining intensity. Strongly positive samples were defined as the high-expression group, while negative and weakly positive samples were considered the low-expression group.

Statistics

Statistical analysis was performed using GraphPad Prism 9 (https://www.graphpad-prism.cn/) and R 4.2.2 (https://www.r-project.org/). Continuous variables with normal distribution and equal variance between binary groups were compared using Student's *t*-test; otherwise, the Wilcoxon rank-sum test was used, such as the differences between high- and low-risk groups regarding the expression levels of CCDI-related genes and levels of intratumoral infiltrating immune cells. We used the quantile–quantile (QQ) plot to test the normality assumption of data sets, while Levene's test was applied to compare the variances between the two sets of data. Continuous variables with normal distribution and equal variance between ternary and more groups were compared using one-way ANOVA; otherwise, the Kruskal–Wallis test was used. The chi-squared test was used to assess whether there was a difference between multiple overall rates or component ratios. We evaluated the survival data for proportional hazards and linearity for quantitative predictors, the assumptions underlying the Cox regression, before performing univariable and multivariable Cox regression analysis to estimate hazard ratios (HR) and 95% confidence interval (CI) of PCD-related genes against OS, using the "survival" and "survminer" R packages. To evaluate the prognostic models' prediction accuracy prognosis in patients with ESCC, time-dependent receiver ROC curves were generated, and AUC was calculated and plotted using the R packages "pROC", "survivalROC" and "ggplot2".[58] Kaplan–Meier survival curves were plotted to compare OS between the high- and low-risk groups. The difference in OS between these groups was assessed using the log-rank test, which was conducted using the "survival" and "survminer" R packages. The "surv_cutpoint" algorithm in the "survminer" R package was used to determine model cutpoints. Uniform Manifold Approximation and Projection (UMAP) analysis and visualisation in the "umap" R package were used to assess discriminative power. Recall curves were evaluated to assess the precision and recall of the model based on the "modEvA" R package.[59] Correlations between variables were examined using Pearson correlation analysis. Immune cell levels and the immune score of samples were evaluated using "CIBERSORT" and ESTIMATE" R packages and "TIMER 2.0" website". All experiments were repeated at least three times, and the results of continuous variables are presented as mean ± standard deviation (SD). Unless otherwise stated, $P < 0.05$ was considered statistically significant.

Ethics

The Ethics Committee of the Cancer Hospital of Harbin Medical University approved the use of retrospective patient material. Written informed consent was obtained from all participants.

Role of the funders

The funders played no role in the study design, data collection, data analysis, data interpretation, and paper writing.

Results

Identification of genes associated with 14 forms of cell death and establishment of prognostic signatures

First, the signature gene sets of 14 cell death forms were collected from published literature and databases (Supplementary Table S2), including apoptosis (intrinsic and extrinsic), entotic cell death, necroptosis, cuproptosis, oxeiptosis, ferroptosis, alkaliptosis, pyroptosis, parthanatos, autophagy-dependent cell death, lysosome-dependent cell death, netotic cell death, and ICD. The study flowcharts are shown in Fig. 1a and Supplementary Figure S1. The univariate Cox regression was used to filter out genes not significantly associated with OS (adjusted q-values <0.05) from a total of 3518 genes retrieved for 14 forms of PCD. Then, the multivariable Cox regression was used to generate a prognostic gene signature for each form of cell death with the remaining corresponding genes. The expression levels of the genes included in each prognostic signature were compared between normal and tumour tissues, followed by the matching forest plots summarising the results of multivariable Cox regression analysis (Fig. 1b–o).

Evaluation of 14 prognostic models and the CCDI model

The time-dependent ROCs of the 14 prognostic models were plotted (Fig. 2a). Prognostic models with a lower 95% confidence limit of AUC>0.7 for 1, 2, 3, 4, and 5 years were used for the combined analyses. Among various combined models containing 2–4 individual prognostic signatures, the model combining ICD (AUC = 0.800) and necroptosis (AUC = 0.803), named combined cell death index (CCDI), showed the highest predicting accuracy (AUC = 0.834) (Fig. 2b). The CCDI consisted of 16 genes (KIF11, MTOR, PIK3R1, TSC1, HOOK1, ALK, CEACAM1, VIM, CCND1, DPP4, NGFR, RPS24, MEFV, CLU4A, RARG, and SRC). Its time-dependent ROC curves are shown in Fig. 2c.

The Kaplan–Meier survival curves (Fig. 2d) and Uniform Manifold Approximation and Projection

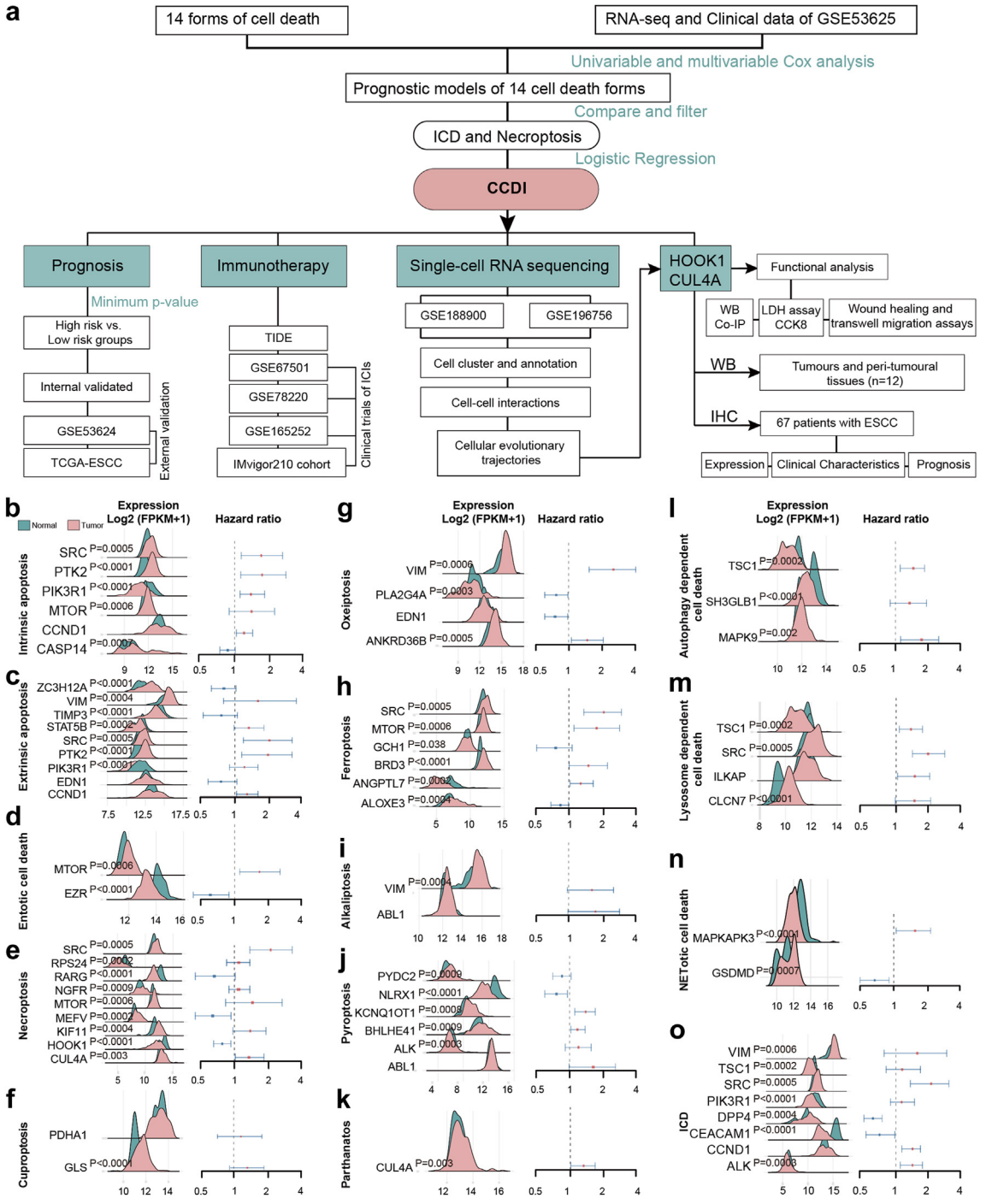

Fig. 1: **Establishment of 14 prognostic models based on different cell death forms.** a. The flowchart of the study. We constructed 14 prognostic models based on genes associated with various cell death forms. b–o. Expression (Normal vs Tumour tissues) (n = 358) and results of multivariable Cox regression analysis for genes included in each prognostic model are shown for different types of cell death, including intrinsic apoptosis (b), extrinsic apoptosis (c), entotic cell death (d), necroptosis (e), cuproptosis (f), oxeiptosis (g), ferroptosis (h), alkaliptosis (i), pyroptosis (j), parthanatos (k), autophagy-dependent cell death (l), lysosome-dependent cell death (m), netotic cell death (n), and immunogenic cell death (ICD) (o) (n = 179). Hazard ratio (x axis) is presented on the logarithmic scale in the forest plots. *P* values for differences in gene expression between tumours and normal tissues were determined by the student t-test. CCDI, combined cell death index; ESCC, oesophageal squamous cell carcinoma; TIDE, Tumor Immune Dysfunction and Exclusion; WB, Western blot; LDH, Co-IP, co-immunoprecipitation; CCK-8, cell counting kit-8; lactate dehydrogenase; IHC, Immunohistochemistry.

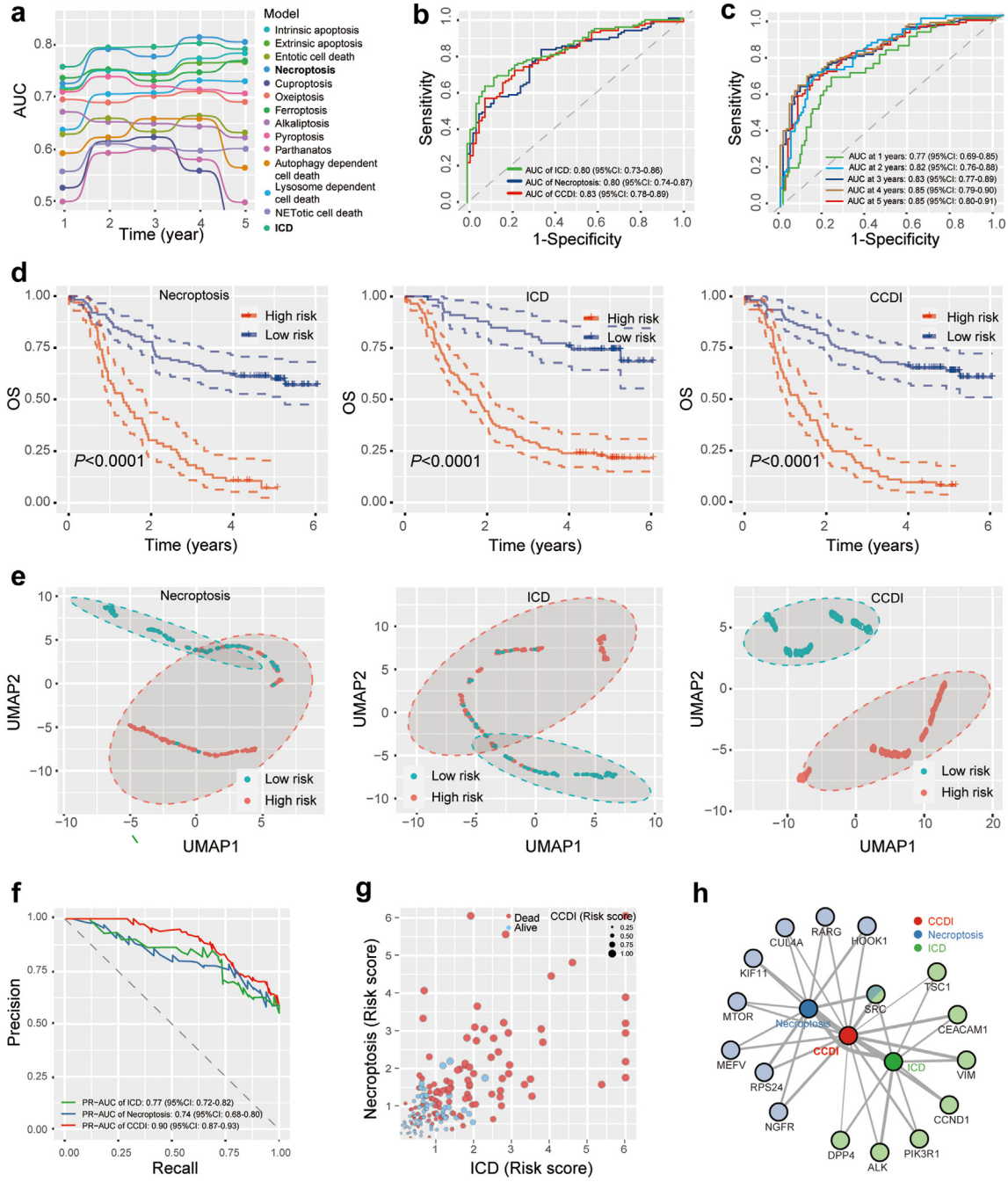

***Fig. 2:* Evaluation of the 14 prognostic models of cell death forms in the training set (GSE53625, n = 179).** a. The area under the time-dependent receiver operating characteristic (ROC) curve for prognosis-predicting models of 14 cell death forms at indicated time points. b. ROC plots of necroptosis, ICD, and combined cell death index (CCDI) models. c. Time-dependent ROC curves for the CCDI. d. The Kaplan–Meier curves for high- and low-risk patient subgroups are presented for the three models (The dotted curves depict the 95% confidence interval for the survival curve, n = 179, log-rank test, $P < 0.0001$). e. Uniform Manifold Approximation and Projection (UMAP) analysis and visualisation estimate the discriminating ability of necroptosis, ICD, and CCDI models for the low- and high-risk groups. f. The precision–recall curves evaluate the prognostic accuracy of indicated models (Recall is the sensitivity while precision means positive predictive value). g. Correlation between necroptosis and ICD risk scores. CCDI increases while necroptosis and ICD risk scores increase. h. The network of genes and the labelled prognostic models. Line weights measure the correlation between individual gene expression levels and the risk score of corresponding risk models, as well as the correlation among the three models concerning the risk score. Pearson correlation analysis was used to assess the correlations (n = 179). AUC, area under the curve; CI, confidence interval; OS, overall survival.

(UMAP) analysis and visualisation (Fig. 2e) showed that the CCDI could better discriminate patients with favourable prognosis from those with poor outcomes compared to the ICD or necroptosis model alone. In addition, the Precision-Recall Curve (PRC) (PR-AUC of necroptosis = 0.74, PR-AUC of ICD = 0.77 and PR-AUC of CCDI = 0.90) was plotted (Fig. 2f). A correlation between necroptosis and ICD risk scores was displayed, and CCDI increased with increasing necroptosis and ICD risk scores (Fig. 2g). These results suggest that the CCDI had higher predicting accuracy for the prognosis and could more precisely distinguish patients at high risk (CCDI >0.64) from those with low risk (CCDI ≤0.64) than the single cell death pattern models. Finally, associations of genes with ICD, necroptosis, and CCDI models were mapped using Pearson correlation methods. Central dark blue, green, and red spots symbolised necroptosis, ICD, and CCID models connected with related genes by the grey lines (Fig. 2h). Line thickness is proportional to the correlation between the expression level of each gene and the risk score of corresponding prognostic models, as well as the correlation among ICD, necroptosis, and CCDI models regarding the risk score (Fig. 2h). We further validated the CCDI model in the TCGA-ESCC (Supplementary Figure S2a, b, e, f) and GSE53624 cohorts (Supplementary Figure S2c, d, g). Similarly, ROC curves, the Kaplan–Meier survival curves, and UMAP analyses indicated that the CCDI outperformed the necroptosis or ICD model alone in predicting prognosis for patients with ESCC.

Immunotherapy response in high- and low-risk groups defined by CCDI

To explore the predictive power of the CCDI model for immunotherapy sensitivity, we analysed the correlation between the CCDI model risk score and 51 immune checkpoints and modulators.[60] The results showed that the CCDI was significantly correlated with a broad spectrum of immune-related genes, indicating the potential immune implications of the CCDI model (Fig. 3a). The Tumor Immune Dysfunction and Exclusion (TIDE) algorithm was applied to predict response to ICIs in the training set (GSE53625). The results showed that the TIDE method could differentiate responders (TIDE score <0) from non-responders (TIDE score>0) (Fig. 3b). The Pearson correlation analysis indicated that the risk score was positively associated with the TIDE score, meaning that patients with low CCDI are more likely to respond to ICIs than those with high CCDI scores (Fig. 3c). Indeed, in the same cohort, the low-risk group had a larger proportion of responders than the high-risk group (Fig. 3d).

We further confirmed the CCDI's capacity to predict the response to ICIs with the IMvigor210 dataset.[30] The phase II IMvigor210 study recruited 220 patients with locally advanced or metastatic urothelial carcinoma who experienced Response Evaluation Criteria In Solid Tumors (RECIST) v1.1 progression after platinum treatments.[30] CCDI score was calculated for each patient in the IMvigor210 dataset based on the coefficients of multivariable Cox regression analysis and expression of the CCDI genes. Patients with CCDI scores >0.64 (the cutoff value established for the training set in early survival analysis) were categorised into the high-risk group and the remaining patients into the low-risk group. The Kaplan–Meier analysis showed that the patients with low CCDI had significantly elongated survival compared with counterparts with high CCDI (Fig. 3e). Among them, 137 patients received one or more doses of atezolizumab, an inhibitor of PD-L1, after initial cancer progression.[30] Encouragingly, we found that a larger percentage of patients achieved CR or PR in the low-risk group than in the high-risk group defined by CCDI (Fig. 3f). Moreover, CR or PR group patients possessed lower average CCDI than patients in the PD group (Fig. 3g). We also validated the predictive value of this CCDI in patients with melanoma treated with anti-PD-1 therapy (pembrolizumab and nivolumab) in the GSE78220 cohort.[31] Compared with the high-risk group, relatively more patients tended to respond to anti-PD-1 treatment in the low-risk group (Fig. 3h and i). Again, in terms of renal cell carcinoma,[32] we observed that patients with low CCDI were more likely to benefit from anti-PD-1 therapy, and the CCDI was lower in the responders (GSE67501) (Fig. 3j and k). The discriminant accuracy of the CCDI in predicting response to ICIs was also confirmed in a clinical trial of resectable oesophageal adenocarcinoma (EAC) with atezolizumab (GSE165252) (Fig. 3l and m).[33] Taken together, these results suggest that the patients with low risk were more sensitive to ICIs, implying that the CCDI may be able to predict sensitivity to ICIs in different types of cancer.

Comparison of tumour immune microenvironment between high- and low-risk groups

Given the differential response to ICIs of the two risk groups, we further explored the underlying mechanisms. GSEA based on ESCC bulk sequencing data (GSE53625) demonstrated that many immune-related pathways were associated with low-risk groups (Supplementary Figure S3a and b). Moreover, using the MCP-counter, recognising ten types of cells in TME, including immune and stromal cells, we detected significant differences in NK cells, B lineage, cytotoxic lymphocytes, and neutrophils between the two groups (Supplementary Figure S3c). As shown in Supplementary Figure S3e, the CIBERSORT algorithm, enumerating 22 immune subsets, uncovered the significant difference in plasma cells, monocytes, activated NK cells, neutrophils, activated dendritic cells, and M2 macrophages between the two groups. Correlations between the CCDI and different types of cell populations are exhibited in Supplemental Figure S3d and f. Again,

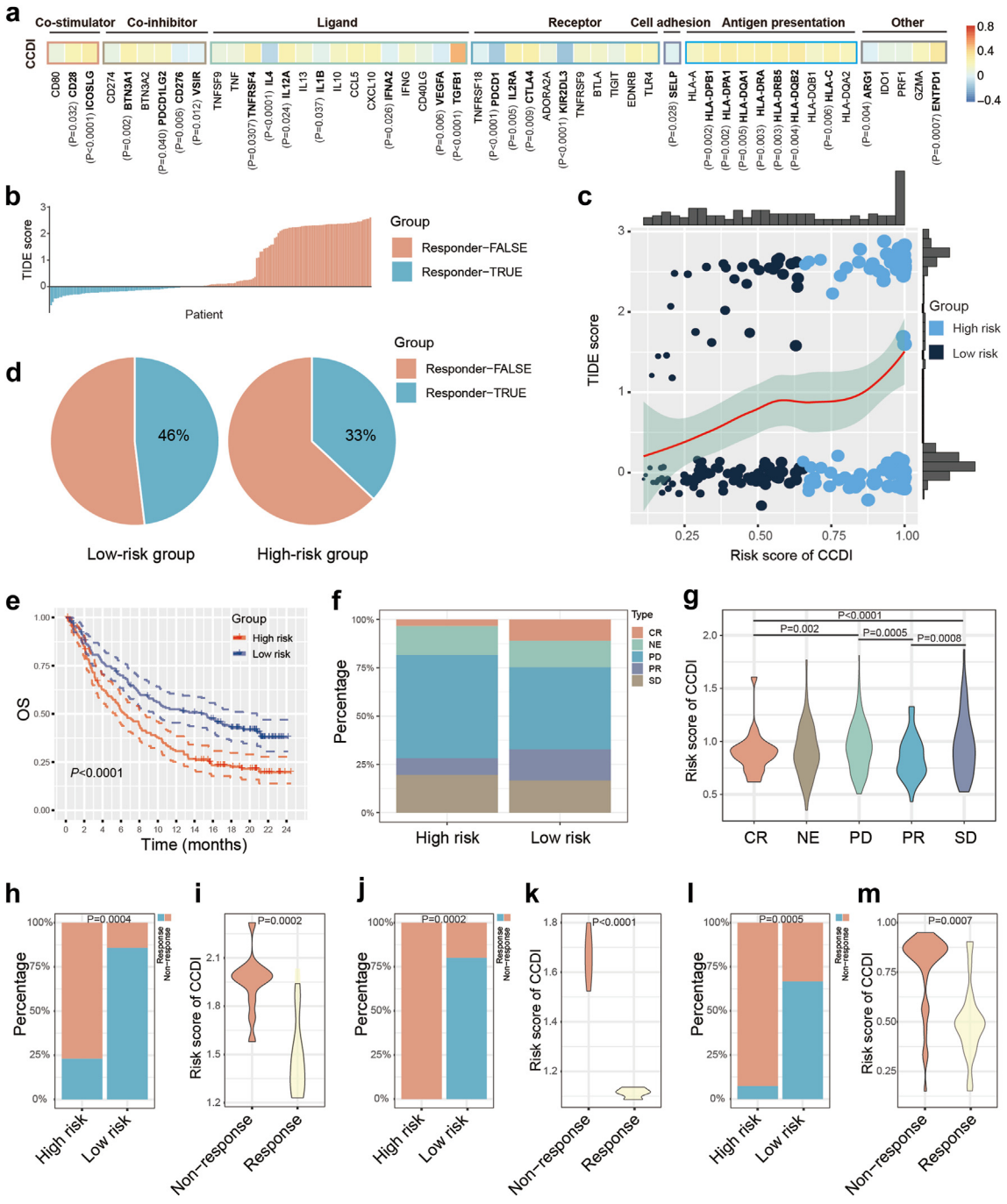

***Fig. 3*: Comparison of the Immunotherapy efficacy between high and low-risk groups defined by the CCDI.** a. Heat map of correlation between the CCDI and immune checkpoints (Blue square represents negative correlation, while red square represents positive correlation) (GSE53625, n = 179). b. Tumor Immune Dysfunction and Exclusion (TIDE) analysis indicated the distribution of responders and non-responders to immune checkpoint inhibitors (ICIs) in the training set (GSE53625, n = 179). c. Correlation of TIDE scores of patients with CCDI (GSE53625, n = 179). d. Percentages of ICI responders in the low-risk group compared to the high-risk group (GSE53625, n = 179). e. Kaplan–Meier OS curves for the CCDI-defined high- and low-risk groups in the IMvigor210 (externally validated, log-rank test, $P < 0.0001$) dataset (n = 220). f, h, j, l. Comparison of the response to anti-PD-L1 treatment in the high-risk and low-risk groups in the IMvigor210 study (Bladder urothelial carcinoma, n = 137) (f), GSE78220 (Melanomas, n = 28) (h), GSE67501 (Human renal cell carcinoma, n = 11) (j) and GSE165252 (resectable oesophageal adenocarcinoma, n = 40) (l) cohorts. g, i, k, m. The differences in CCDI between the high- and low-risk groups of the IMvigor210 (g), GSE78220 (i), GSE67501 (k) and GSE165252 (m) cohorts. Pearson correlation analysis was performed to assess the correlations. Differences in immunotherapy response between high and low-risk groups were compared using the chi-square test. Differences in CCDI between the two groups were analysed using a student *t*-test, and one-way ANOVA was used for the comparisons among three or more groups.

other methods, such as CIBERSORT-ABS, EPIC, QUANTISEQ, TIMER, and XCELL, also confirmed the distinct forms of immune cell infiltration between the two groups and the correlation between the risk score and the immune subsets (Supplemental Figure S4a and b). Finally, analyses with the ESTIMATE algorithm revealed that the immune score in the CCDI-defined low-risk group was significantly higher than those in the low-risk group in the training set and two validation sets (Supplemental Figure S4c–e). The difference in immune score may partially explain the discrepancy in response to ICIs between the two groups.

Different tumour-associated pathways among the high- and low-risk groups

GSVA was used to explore further the molecular and cellular characteristics of the two different risk groups. Compared to the low-risk group, the high-risk group had higher enrichment scores in tumour-related signalling pathways, including EMT, G2M checkpoint, cell cycle, E2F targets, TGF-β signalling, NOTCH signalling, HEDGEHOG signalling, ADHERENS junction and Wnt/β-catenin pathway, while lower scores in necroptosis, pyroptosis, and p53 signalling pathways (Supplementary Figure S5a–m).

Establishment of ESCC cell atlas using single-cell RNA transcriptome

Although our findings are interesting, all analyses were conducted based on the bulk transcriptomes. These results conveyed mixed information on diverse cells but failed to delineate the cellular diversity of the TME in a single-cell resolution. Therefore, we further analysed the importance of the CCDI gene by taking advantage of the published single-cell transcriptome data (GSE196756). After multiple quality control and filtering steps, we obtained an expression matrix of 24,171 genes retrieved from 36,515 single cells. Using typical individual marker genes, the total cells were clustered into eight major cell types, including epithelial cells (epithelial and ESCC cells), immune cells (T cells, B cells, monocytes, and dendritic cells), stromal cells (fibroblasts and endothelial cells), and erythrocytes (Fig. 4a and b). For instance, fibroblasts were characterised by high expression of several extracellular matrix genes, fibronectin 1 (FN1), decorin (DCN), collagen type 1 (COL1A1), and COL12A; meanwhile, T cells preferentially expressed CD3 delta subunit of T-cell receptor complex (CD3D) and T cell surface antigen CD2 (CD2). The same goes for identifying B cells (IL3RA, MS4A1, and CD79A) and monocytes (MS4A7, FCGR3A, LYZ, and CD14). The proportion of epithelial, immune, and stromal cells varied greatly between paired normal and tumour tissues (Fig. 4c). Next, the results of intercellular communication analysis showed that ESCC cells had vital interaction with immune and stromal cells (Fig. 4d and e). These results suggest a mutual regulation between tumour cells and the immune microenvironment.

It is believed that tumour cells, immune cells, and stromal cells interact dynamically and reciprocally in the tumour microenvironment. Their intricate communication and joint contributions consequently lead to the tumour fate decision. CellChat, a newly published machine learning method, allows us to quantitatively extrapolate intercellular communications from single-cell RNA-sequencing (scRNA-seq) data based on ligands, receptors, and their cofactors.[37] The circle plots visualised comprehensive cell-to-cell interaction networks among tumour cells, T cells, B cells, monocytes, dendritic cells, fibroblasts, and endothelial cells by the number of interactions and the interaction strength (Fig. 4d and e).

We next extrapolated incoming and outgoing signals for different cell types in the TME using CellChat. All kinds of cells can synthesise and secret various cytokines or ligands as signal senders; meanwhile, they sense extracellular ligands via receptors as signal receivers. The crucial signals mediating communications among different cell types are exhibited in Fig. 4f. Collectively, the ligand–receptor interaction among different cell types in the TME highlighted the importance of each cell subpopulation for tumour development.

Identification of dynamic CCDI genes during the transition of cell states

Next, by plotting single-cell trajectories, we attempted to investigate whether the CCDI genes contribute to cell fate decisions in infiltrating immune, stromal, and ESCC cells (GSE196756). First, the seven cell populations were divided into subsets using the "singleR" R package and marker genes collected in published studies (upper panels of Fig. 5a–g). We ranked cells with the "Monocle2" R package within original groups based on cell subtypes to establish their single-cell motility trajectories. The starting point of the timeline trajectory of each cell population is shown by arrows (middle panels of Fig. 5a–g). For instance, in the case of T cells, the transition might initiate in naïve T cells (blue), which then develop into $CD4^+$ T cells (red) and $CD4^+$ memory T cells (green) (upper and middle panels of Fig. 5b). We identified that levels of PIK3R1, RPS24, and VIM dynamically altered along the differentiation process of T cells (lower panel of Fig. 5b), suggesting that these genes might be somehow related to the cell fate decision of these cells. Overall, we found that RPS24 and VIM might regulate the cell states of all analysed cell populations anyhow. In addition, cyclin D1 (CCND1) may also execute a particular function in the dynamic transitions of fibroblasts and endothelial cells (Fig. 5e and f). We also noticed that CUL4A was implicated in the differentiation process of ESCC cells (Fig. 5g). However, these results should be interpreted cautiously. For instance, the $CD4^+$ cell subpopulations based on the machine learning strategy should be

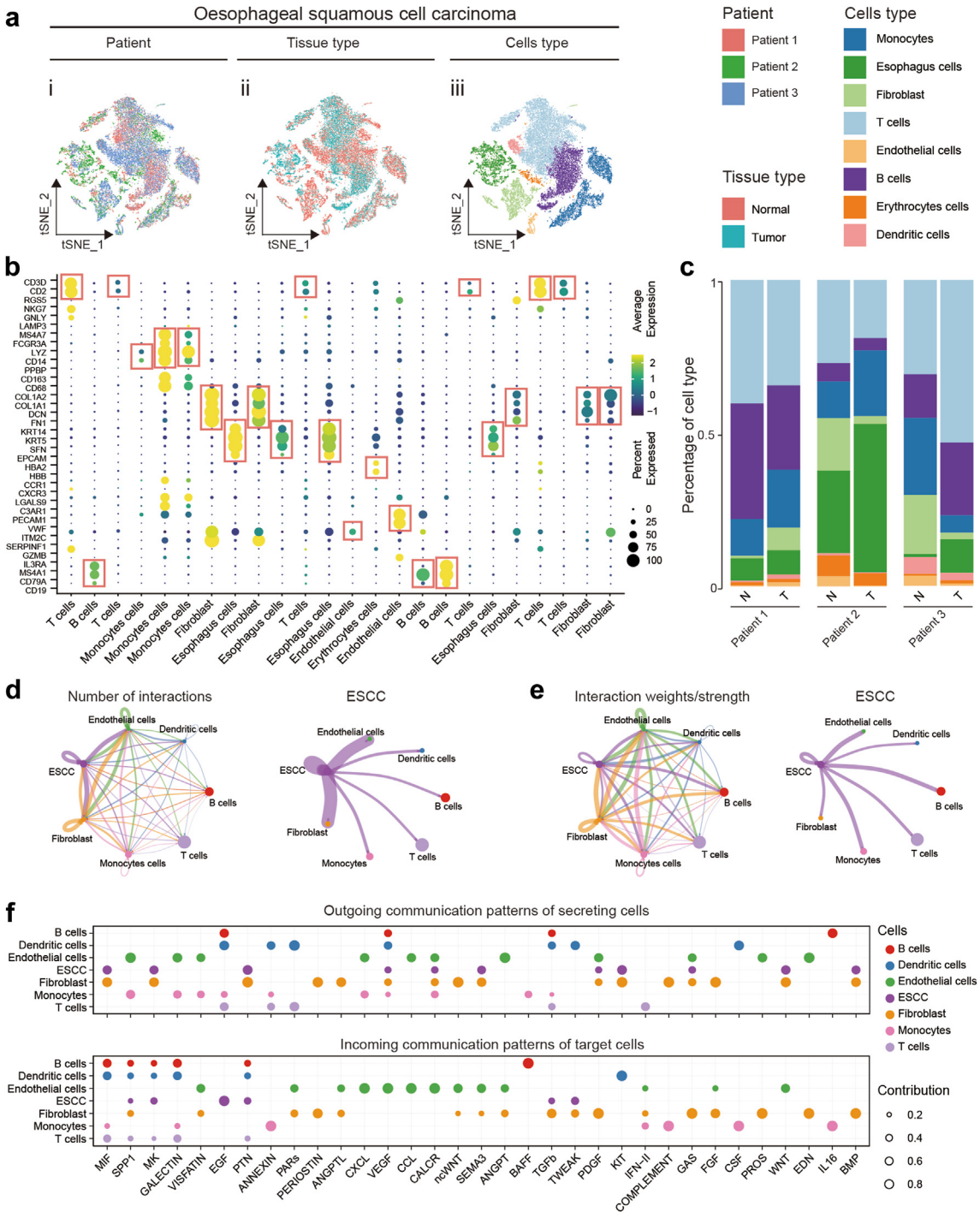

Fig. 4: **Clustering and annotation of single-cell RNA sequencing data in** GSE196756 **(n = 6).** a. The t-distributed stochastic neighbour embedding (t-SNE) plot of patients, tissue types, and the eight identified main cell types in ESCC tumours and normal oesophageal tissues. b. Bubble plot showing 36 marker genes expressed in the eight-cell types. The size of the bubbles represents the proportion of cells expressing marker genes, and the spectrum of colours indicates the average expression level of marker genes (log1p transformation). c. Histograms display the percentages of different cells across normal and tumour tissues of the oesophagus. d-e. The number of interactions (d) and interaction weights/strength (e) of cell and cells in the tumour microenvironment of ESCC. The colour and width of the lines represent the number of interacting pairs between cell types. f. The bubble plots indicate the key outgoing and incoming signalling patterns of the cell, respectively. The size of the dots is proportional to the calculated contribution fraction in cellular communication, with higher contribution fractions representing signalling pathways that are more abundant in cellular interactions.

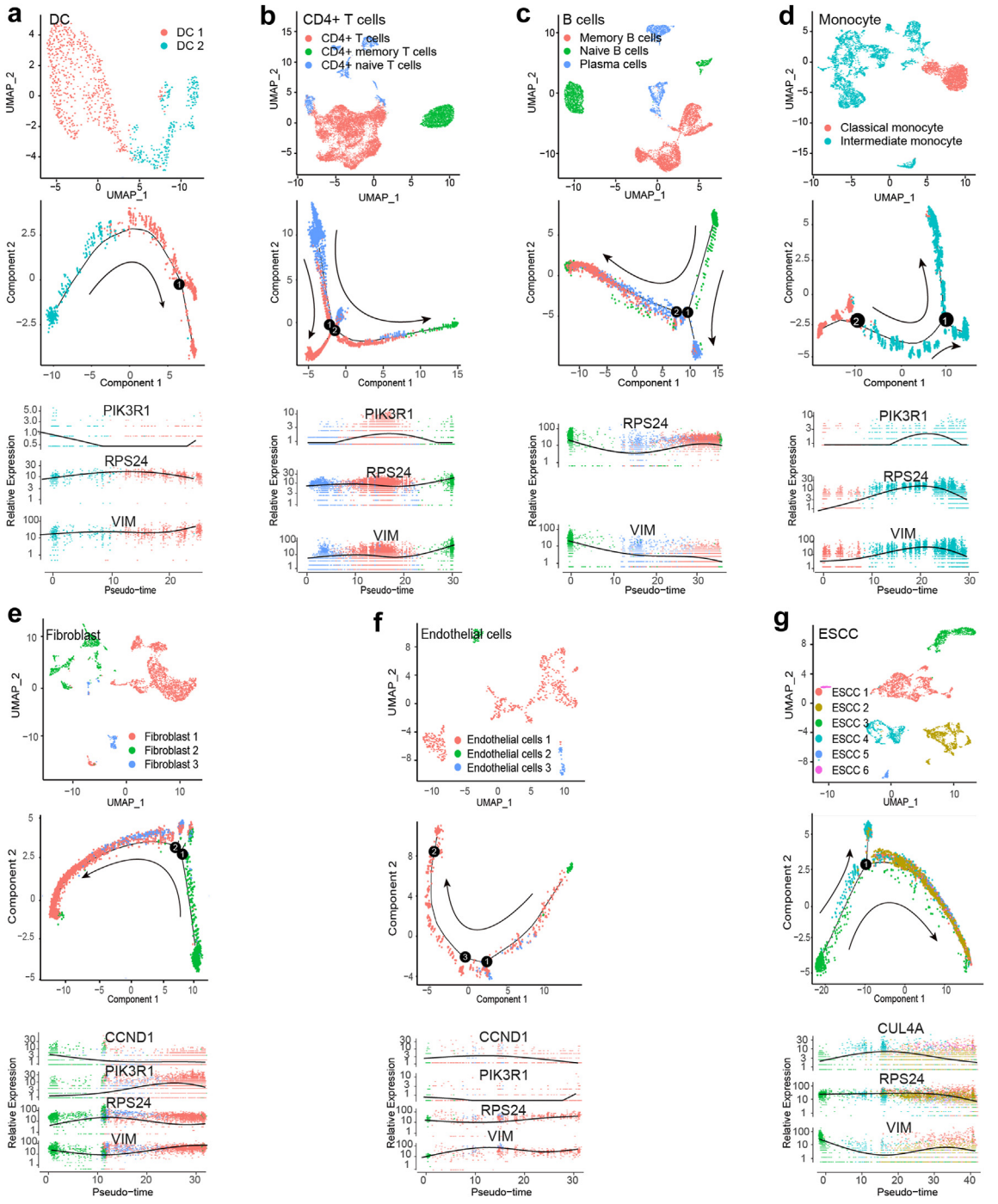

Fig. 5: **Pseudo-time analysis of each cell type and dynamic changes of CCDI- gene expression in trajectories in the training set (GSE196756, n = 6)**. a–g. Cell subpopulations (upper panels), single cell motility trajectories (middle panels), and dynamic genes during the cell differentiation (lower panels) were visualised for dendritic cells (DC) (a), CD4+ T cells (b), B cells (c), monocytes (d), fibroblasts (e), endothelial cells (f), and ESCC cells (g). UMAP plots show the main subclusters of cells. The "Monocle2" algorithm was used to perform trajectory plots for cells and determine dynamic genes. Each dot indicates a single cell coloured by its cluster, and the solid black line shows the LOESS fit in the lower panels.

validated with T cell receptor sequencing (TCR-seq). We obtained another ESCC scRNA-seq dataset (GSE188900) with an expression matrix of 23,160 genes retrieved from 52,772 single cells (Supplement Figure S6). We confirmed the importance of RPS24, VIM, and PIK3R1 in the decision-making of cell fates (Fig. 6). Interestingly, the results from the new dataset suggested that besides CUL4A, HOOK1 may also be critical for ESCC cell transition (Fig. 6g).

In vitro functional analyses of HOOK1 and CUL4A

Hook Microtubule Tethering Protein 1 (HOOK1) is a member of the hook family of coiled-coil proteins. It can bind to microtubules and organelles and may bridge the endocytic membrane trafficking and the microtubule cytoskeleton. Cullin 4A (CUL4A) is a critical component of multiple cullin-RING-based E3 ubiquitin-protein ligase complexes, regulating the ubiquitination of substrates. Given the functional significance of HOOK1 and CUL4A in ESCC prognosis and the regulation of tumour cell fates revealed by the bioinformatic analysis, we investigated the *in vitro* function of HOOK1 and CUL4A. We examined the expression levels of HOOK1 and CUL4A in oesophageal epithelial cells and ESCC cell lines. KYSE150 and KYSE410 cells with relatively low HOOK1 and CUL4A levels were used for the gain-of-function analysis (Fig. 7a). RT-qPCR (Fig. 7b, top) and Western blot (Fig. 7b, bottom) assays were performed to confirm the efficiency of gene manipulation. We next demonstrated that cisplatin could elicit necroptosis in ESCC cells (Fig. 7c) and use it as a necroptosis inducer. Ectopic expression of HOOK1 induced necroptosis in ESCC cells as indicated by increased levels of RIPK1, p-RIPK3, and p-MLKL, which was attenuated by several necroptosis inhibitors in a concentration-dependent manner, such as necrostain-1 (Nec-1), a potent anti-MLKL drug necrosulfonamide (NSA), and a more specific anti-pRIPK1 drug RIPA-56 (Fig. 7d–f). The hallmark of necroptosis is the formation of the necrosome, a complex consisting of RIPK1 and RIPK3, and the recruitment and phosphorylation of MLKL. Our Co-IP results demonstrated that enforced expression of HOOK1 prompted the interaction of RIPK1, RIPK3, and MLKL, suggesting increased necrosome complexes in the ESCC cells (Fig. 7g). Moreover, overexpression of CUL4A reduced necrosome formation (Fig. 7h). These data further confirmed that HOOK1 and CUL4A promoted and reduced necroptosis in ESCC cells. LDH assay substantiated that HOOK1 overexpression-mediated cell injury could be reversed by Nec-1, NSA, and RIPA-56 (Fig. 7i–k), while CUL4A overexpression significantly reduced cisplatin-induced necroptosis in ESCC cells (Fig. 7l), suggesting that the two genes regulate necroptosis. In addition, we investigated the effects of HOOK1 and CUL4A on the proliferation and migration of ESCC cells. Forced expression of HOOK1 inhibited proliferation and migration of ESCC cells as shown by the CCK, transwell migration, and wound healing assays (Fig. 7m, o, q), while CUL4A exerted an inverse influence on cancer cells (Fig. 7n, p, r). These results unveiled the tumour-suppressing and promoting potentials of HOOK1 and CUL4A in ESCC cells by regulating cancer cell necroptosis, proliferation, and migration, respectively.

Validation of CUL4A and HOOK1 in clinical specimens

In addition, we validated the expression of these two genes in the samples of patients with ESCC. The Western blot results showed that HOOK1 was highly expressed in peri-tumoral tissues compared to matched tumour tissues collected from 12 patients. Meanwhile, a reverse expression trend was found for CUL4A, suggesting a tumour-promoting potential of this gene (Fig. 8a). We also performed immunohistochemistry (IHC) staining on tumour tissues from 67 patients with ESCC along with 10 peri-tumoral tissues (Fig. 8b and c, Supplement Figure S7). HOOK1 was found to predominantly localise in the cytoplasm of epithelial cells and down-regulated in peri-tumoral tissues (Fig. 8b, d). In addition, HOOK1 expression levels were further decreased in tumours with low/medium degree of differentiation compared to highly differentiated tumours (Fig. 8e) and were not associated with the clinical stage (Fig. 8f). CUL4A was present in the nucleus and cytoplasm of epithelial cells and up-regulated in tumour tissues (Fig. 8c, h). CUL4A was associated with neither the differentiation degree nor the clinical stage of ESCC (Fig. 8i and j). Moreover, patients with ESCC were dichotomised concerning expression levels of HOOK1 or CUL4A. The Kaplan–Meier survival analyses indicated that patients with $HOOK^{high}$ tumours exhibited significant survival advantages over those with $HOOK^{low}$ tumours (Fig. 8g). In contrast, patients with high CUL4A expression had a poorer prognosis than those with low gene expression (Fig. 8k). Combined analysis elucidated that patients with ESCC with $HOOK^{low}$/$CUL4A^{high}$ tumours have the worst OS (Fig. 8l). Univariate and multivariable COX regression analyses identified HOOK1 (Fig. 8m) as an independent predictor for prognosis in ESCC. Collectively, these results reaffirm that HOOK1 and CUL4A play an essential role in the development of ESCC.

Discussion

PCD occurs in an orderly and controllable manner to maintain homeostasis, regulated by given signalling pathways. Over ten types of PCDs have been recognised to date.[4] Moreover, all kinds of cell death usually end up with an immunological consequence. On the one hand, pro-inflammatory cytokines or antigens released by dead cells undergoing some PCDs like pyroptosis can

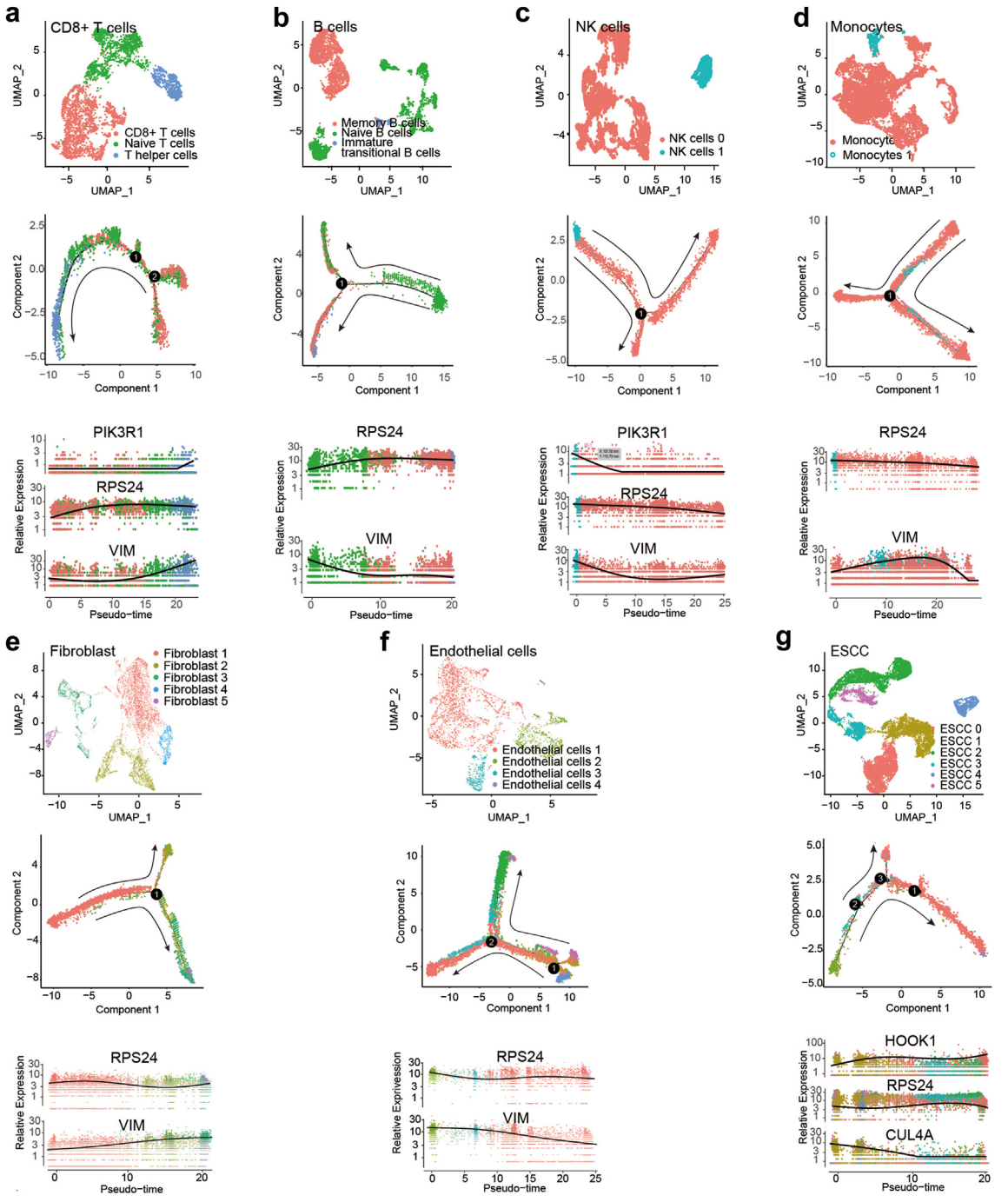

Fig. 6: **Validation of the implications of CCDI-gene in cell state transition with** GSE188900 **(n = 7)**. a–g. T cells (a), B cells (b), NK cells (c), Monocytes (d), fibroblast (e), endothelial cells (f), and ESCC cells (g) were divided into subgroups (upper panels), shown in single cell motility trajectories (middle panels). The dynamic genes during the cell differentiation (lower panels) were also determined for these cell populations. Each dot indicates a single cell coloured by its cluster. The solid black line represents the LOESS fit in the lower panels.

arouse inflammation and specific immune responses, called immunogenic cell deaths.[61] On the other hand, when apoptotic and dead cells are phagocytised, cells die quiescently without activating inflammatory or immune reaction cascades. Because of the importance of ICD in tumour progression and immunotherapy

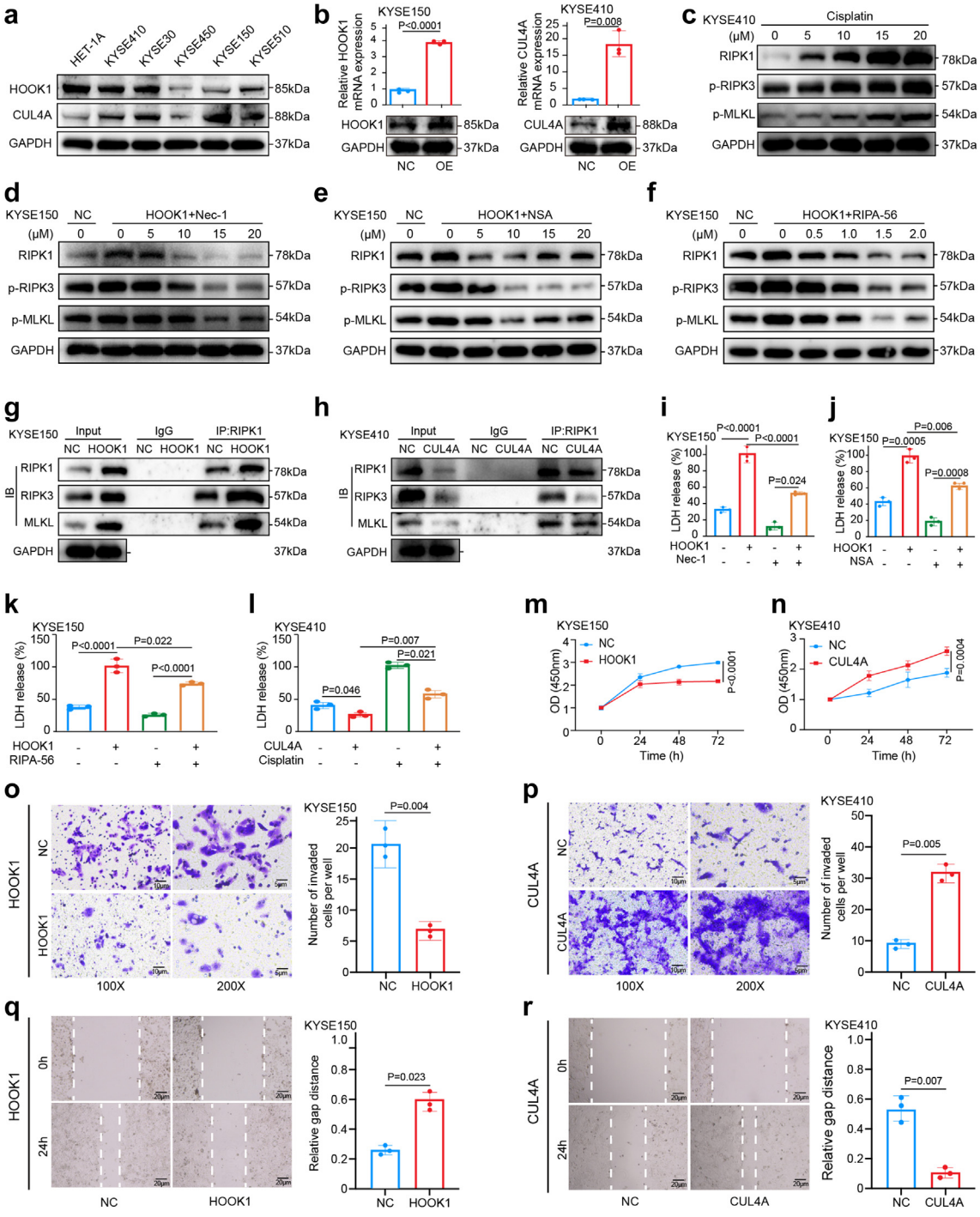

***Fig. 7*: Impacts of HOOK1 and CUL4A on necroptosis, proliferation, and migration of ESCC cells.** a. Differential expression of HOOK1 and CUL4A in normal oesophageal epithelial cells and ESCC cells by Western blot analysis. b. The overexpression efficiency of HOOK1 and CUL4A was examined using qRT-PCR (upper panel) and Western blot analysis (lower panel). c. KYSE410 cells were treated with increasing concentration of cisplatin for 24 h and then were subjected to Western blot analysis for necroptosis biomarkers. d-f. ESCC cells (KYSE150) with HOOK1 overexpression were treated with the indicated concentrations of different necroptosis inhibitors for 24 h, including necrostatin-1 (Nec-1), necrosulfonamide (NSA), and RIPA-56. Western blot analysis was conducted to examine necroptosis biomarkers. g, Co-IP showed that HOOK1 facilitated the precipitation of RIPK3 and MLKL with RIPK1. h, Co-IP indicated that HOOK1 reduced the RIPK3 and MLKL interacting with RIPK1. i–l. The LDH release assay was used to quantify the effect of Nec-1 (15 μM) (i), NSA (10 μM) (j), and RIPA-56 (1.5 μM)

response, we also consider ICD as a type of cell death in our analysis.

There is no doubt that the primary goal of most cancer treatments is induced neoplastic cell death. However, the tumour is complex and intriguing, and PCDs could play dual roles in cancer depending on the context.[16] For instance, substantial evidence has shown that necroptosis, pyroptosis, and ferroptosis could enhance tumour immunogenicity; paradoxically, the same types of death can lead to immune suppression and tumour progression.[16] Entosis also plays a context-dependent role in tumorigenesis. By engulfing cells, it may supply nutritional ingredients for tumour growth but may also facilitate healthy neighbouring cells to remove malignant cells.[62,63] Because of the pivotal and intriguing roles of various PCDs in cancer, abundant multi-gene signatures based on individual PCD forms have been developed and shown great promise in predicting clinical outcomes, drug resistance, and response to ICIs in cancer, such as pyroptosis, ferroptosis, autophagy, ICD, and the recently emerged cuproptosis.[18–21,23,64,65] However, the different PCDs are not absolutely mutually exclusive. Many redundancies and crosstalks have been observed among the signalling pathways regulating these cell death modalities, suggesting they may collectively affect tumorigenesis and progression.[16] Therefore, a predictive signature integrating information on multiple PCDs may better characterise the tumour status. By developing and comparing prognostic gene signatures derived from each type of PCD-related genes with public ESCC bulk RNA-Seq data, we found that ICD- and necroptosis-related models had superior prognostic ability compared to other cell death models. Moreover, the combination of these two models, CCDI, exhibited the best performance in predicting prognosis. Two external datasets validated these results, confirming the CCDI's reliable prognostic power and generalizability.

Given the AUC values, the CCDI with an AUC >0.8 performed better than many published prognostic signatures in ESCC, including the lymph node metastasis-associated gene signature,[66] the magnetic resonance radiomic signature,[67] ferroptosis signature,[68] autophagy-related gene signature[65] and immune-related genes signature.[62] The literature search retrieved only one analysis based on multi-PCD.[69] Zou et al. collected programmed cell death genes from 12 PCDs and pooled 1078 genes. After several filtering processes, the Lasso-Cox regression model was applied to establish a 12-gene signature out of 18 PCD genes.[69] The authors reported a decent performance of this diverse PCD signature in predicting prognosis and drug sensitivity in patients with resectable triple-negative breast cancer.[69] The finding also demonstrated that the comprehensive analysis of PCDs is a promising strategy for developing accurate predictive models in cancer. Overall, it is suggested that the combined multi-cell death forms model can further improve the prognostic prediction accuracy and address the lopsidedness and limitations of a cell death pattern.

ICIs are one of the revolutionary advances in cancer management. The FDA has approved several ICIs to treat various cancers, including ESCC, in the neo-adjuvant setting or as the first-line therapy.[2] However, ICIs can only achieve reliable and sustainable responses in a proportion of patients with cancer. Therefore, intensive efforts have been made to develop accurate biomarkers for selecting patients who may benefit from the administration of ICIs. Besides PD-L1 expression by IHC, tumour mutation burden (TMB), and microsatellite instability (MSI),[3] physicians still called for better biomarkers to facilitate decision-making on whether to prescribe ICIs to a patient with cancer. To extend the application of the CCDI, we further explored its predicting potential for immunotherapy sensitivity. Using the TIDE database,[17] we found that patients with ESCC in the high-risk group classified by CCDI were prone to resist ICIs compared with patients in low-risk group, with a positive correlation between TIDE and risk score. The CCDI's predicting accuracy was further validated in platinum-treated locally advanced and metastatic urothelial carcinoma,[30] melanoma,[31] renal cell carcinoma,[32] and EAC.[33] In the IMvigor210 study,[30] the CCDI could divide patients with urothelial carcinoma into low and high-risk groups with significantly different survival, suggesting the prognostic value of CCDI in cancers other than ESCC. Moreover, among these patients with urothelial carcinoma, a larger fraction of patients in the low-risk group gained clinical benefits from anti-PD-L1 therapy than in the high-risk group, as indicated by the ratio of CR and PR.[30] In melanoma[31] and renal cell carcinoma,[32] patients in the low-risk group were more likely to experience an anti-PD-1 response. CCDI also showed predictive values in patients with EAC treated with anti-PD-L1 therapy.[33] These results suggest that the CCDI can discriminate patients sensitive to ICIs from non-responders.

In addition, we validated the relationship between the CCDI model and immune cell infiltration based on bulk sequencing data from ESCC. GSEA analysis

(k) on HOOK1 overexpression-mediated cell damage and impacts of CUL4A overexpression on cisplatin (15 μM)-caused necroptosis (l). m-n. The effects of overexpression of HOOK1 (m) and CUL4A (n) on the proliferation of ESCC cells by CCK-8 assay. o-r. The effects of overexpression of HOOK1 (o, q) and CUL4A (p, r) on cell migration ability by transwell assay (scale bar = 5 μm) and wound healing assay (scale bar = 20 μm). The data are presented as the means ± standard deviations (SD) of three independent experiments. The *P* value was determined using the student *t*-test.

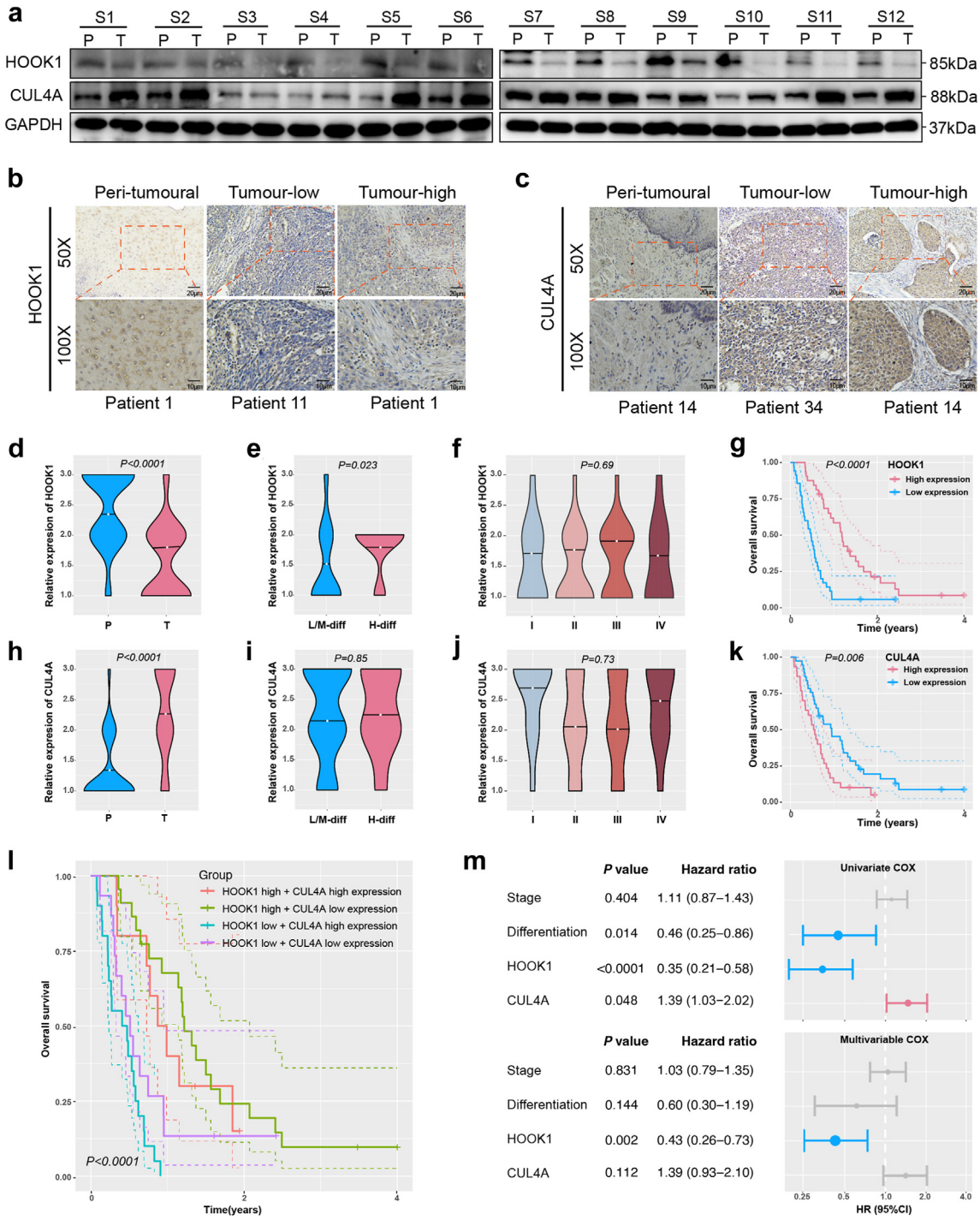

***Fig. 8:* Validation of expression and prognostic potential of HOOK1 and CUL4A in Clinical specimens**. a. Western blot results showed the differential expression of HOOK1 and CUL4A in tumours and matched peri-tumoral tissues from 12 patients. b-c. Representative images of immunohistochemistry (IHC) staining showing high and low expression levels of HOOK1 (b) and CUL4A (c) in peri-tumoral and tumour tissues of indicated patients with ESCC (scale bars = 10 μm and 20 μm for 100x and 50x, respectively; n = 67). d-g. Relationship between the expression level of HOOK1 and tissue type (d), tumour differentiation degree (e), clinical stage (f), and overall survival (g) in patients with ESCC. h-k. Relationship between the expression level of CUL4A and tissue type (h), degree of tumour differentiation (i), clinical stage (j), and overall

showed that immune-related pathways were mainly enriched in the CCDI-defined low-risk group. Additionally, many immune infiltration prediction algorithms disclosed differential immune cell infiltrations between low- and high-risk groups. We also found that patients in the low-risk group had higher immune scores than those in the low-risk group across the training and two validation sets. The association between the immune scores and the infiltrating leukocytes is observed across various tumour types.[51] ICIs may show enhanced efficacy in tumours with intrinsically high levels of infiltrating leukocytes. However, the capacity of the ESTIMATE immune scores to predict immunotherapy response in cancer is controversial.[70–74] Gao et al. observed that the low-risk group classified by a novel pyroptosis-related signature had higher ESTIMATE immune scores and exhibited better responses to ICIs than the high-risk group in oral squamous cell carcinoma.[70] In another study, Liu et al. built a prognostic signature with seven colorectal cancer liver metastases (CRLM)-associated genes. The low-risk group responded more to ICI than the high-risk group. However, there was no difference in the ESTIMATE immune scores between the two groups.[74] In the future, optimal predicting biomarkers should not only concern the composition of the immune infiltrates and the feature of the inflammatory response but also disclose heterogeneity in immunological composition, spatial distribution and function.[75] Finally, GSVA indicated that compared to the low-risk group, the high-risk group had higher enrichment scores in tumour-related signalling pathways. Overall, the differences in intratumoral infiltrating immune cells and activities of the crucial signalling pathways may partially explain the different responses to ICIs between the two groups.

Applications of single-cell RNA-Seq have deepened our understanding of ESCC TME.[35,76] Zheng et al. investigated the immune landscape of the TME at single-cell resolution. They substantiated an immunosuppressive environment in ESCC, such as the presence and dominance of exhausted cytotoxic cells, regulatory T cells (Tregs), M2 polarised macrophages, and continuous progression of CD8+ T cells into an exhausted type.[35] Neoadjuvant chemoradiotherapy (neoCRT) followed by surgery has been widely used to manage patients with locally advanced resectable ESCC. Wen et al. found that neoCRT led to fundamental changes in the immune portraits of TME by analysing and comparing scRNA-seq profiles of paired pre- and post-neoCRT ESCC specimens.[76] Single-cell technologies enable precisely dissecting dynamic changes of biological processes, cell states, and gene expression in an individual cell type among heterogeneous cell populations in TME. Moreover, the dramatic advances in bioinformatic techniques allow us to visualise the communication among different types of cells. Using two scRNA-seq datasets, we unveiled a complex cell communication network in the TME of ESCC, confirming that ESCC development and progression are inextricably linked to immune cells and stromal cells.

Next, we analysed the functional implications of 16 CCDI genes using two scRNA-Seq datasets. Single-cell trajectories were developed to uncover the association between gene expression changes and cell fate decisions, assuming that most cell state transitions concur with the featured gene expression change forms.[55,77] Based on single-cell RNA-Seq data, Monocle 2, involving the 'pseudo-temporal ordering' algorithm, can rank and arrange individual cells in the trajectories according to their states during the differentiation process and other biological process transitions.[55] We performed a pseudo-temporal developmental trajectory analysis of tumour cells, four principal immune cells, and two stromal cells in the TME. We found that the expression of many CCDI genes kept changing during the differentiation of tumour, immune, and stromal cells, including PIK3R1, RPS24, VIM, CCND1, CUL4A, and HOOK1. These results indicated that some CCDI genes might regulate oesophageal carcinogenesis and progression and modulate immune cell function in the TME.

We further validated the regulatory role of CUL4A and HOOK1 in necroptosis in ESCC cells since these two genes may regulate the malignant differentiation of ESCC cells; the clinical relevance of the two genes were also studied in our in-house ESCC samples. Our results elucidated that expression levels of HOOK1 and CUL4A are significantly down- and up-regulated in ESCC, respectively, compared with normal tissue. The prognostic values of HOOK1 and CUL4A were also confirmed, alone or in combination. Patients with ESCC with $HOOK1^{high}/CUL4A^{low}$ tumours survive for the longest time and have much better survival than those with $HOOK1^{low}/CUL4A^{high}$ tumours. Survival analysis revealed that HOOK1 could be an independent protective factor for the prognosis of ESCC, while patients with high CULA4-expressing tumours had a poor prognosis. The study on the relationship between HOOK1 and cancer is very limited. However, the findings of several studies are consistent with ours. HOOK1 is known to bind to

survival (k) in patients with ESCC. l. Kaplan–Meier curves for patients with ESCC with different expression patterns of HOOK and CUL4A. m. Results of univariate and multivariable Cox analyses of characteristic clinical factors, HOOK1 and CUL4A in ESCC. The x-axis shows the HR (logarithmic scale) in the forest plots. Differences in gene expression between two groups were analysed using the student *t*-test; one-way ANOVA was adopted, while three or more groups were compared. The Kaplan–Meier curves were analysed using the log-rank test. HR, Hazard ratio.

microtubules, which is implicated in dynamic changes of the microtubule cytoskeleton, endocytic trafficking, and cell differentiation. Cao et al. reported that patients with thyroid carcinoma having high HOOK1 expression in tumours displayed significantly longer OS than those with HOOK1 low-expressing tumours.[78] Two preliminary studies confirmed the oncogenic role of CUL4A in ESCC. Nakade et al. demonstrated that the knockdown of CUL4A inhibited ESCC cell proliferation and led to cell cycle arrest at the G1 phase.[79] They also reported the association of CUL4A with poor prognosis in ESCC. Moreover, evodiamine (Evo), a small molecule extracted from a traditional Chinese herb, was shown to cause M-phase cell-cycle arrest in ESCC by inactivating CUL4A E3 ligase.[80] Taken together, these results suggested that HOOK1 and CUL4A contribute to tumorigenesis in opposite directions, and these two genes can collaboratively predict the prognosis of ESCC. However, the effects of HOOK1 and CUL4A on necroptosis should be further explored.

This study has several limitations. First, the available ESCC scRNA-seq datasets are very few and have small sample sizes. In the future, ESCC scRNA-seq datasets with larger sample sizes should be analysed to validate our findings drawn from GSE196756 (n = 6) and GSE1888900 (n = 7). Second, it should be noted that the key effectors involved in programmed cell death pathways are mostly regulated at a post-translational level. Therefore, post-translational levels of these molecules are critical in maintaining cell functions and should be considered. However, in this study, we screened PCD-related genes solely depending on the RNA-seq dataset since no corresponding proteomics data are available. In the future, the analysis should be improved by integrating RNA-seq data in combination with proteomics data (e.g., single-cell proteomic information) when possible. Third, at the beginning of the study, we used univariable Cox analysis against OS to screen significant prognostic genes from all candidate genes of 14 cell death forms. Therefore, only genes with significant prognostic value were maintained to develop the predictive model. As a result, genes closely related to cell death but with little prognostic values were excluded, such as RIPK1, RIPK3 and MLKL genes that tightly regulate necroptosis. Fourth, although we conducted internal and external validations for the CCDI, only two independent validation sets were included. More eligible ESCC data sets should be used for validation in the future. Finally, we only validated the CCDI's value for immune therapy in datasets of advanced metastatic urothelial carcinoma, ccRCC, melanoma, and EAC, and the validation should be carried out in ESCC cohorts treated with anti-PD (L)1 or anti-CTLA4.

In conclusion, the CCDI model could assess prognosis and immunotherapy efficacy in cancer. Furthermore, HOOK1 deficiency and CUL4A overexpression in the CCDI model contributed to ESCC development and showed promise for predicting tumour progression.

Contributors

All authors contributed to the study's conception and design. Data preparation, collection and analysis were performed by Kui Cao, Jinhong Zhu, Jianqun Ma, Yanqiao Zhang, Jinfeng Zhang, Yingnan Yang, Xiaodong Ling, Luquan Zhang, Cuicui Qi, Shenshui Wei and Mengdi Lu. Jinhong Zhu and Mengdi Lu accessed and verified the underlying data. Reconciliation of underlying data were solved by Jianqun Ma and Jinhong Zhu. The draft of the manuscript was written by Jinhong Zhu, Kui Cao, and Jianqun Ma. All authors commented on previous versions of the manuscript. All authors read and approved the final manuscript.

Data sharing statement

Public data used in this work can be acquired from the TCGA Research Network portal (https://portal.gdc.cancer.gov/) and Gene Expression Omnibus (GEO, http://www.ncbi.nlm.nih.gov/geo/). The raw experimental data and analysis codes supporting the conclusions of this article will be made available by the corresponding author.

Declaration of interests

There was no competing interest to disclose.

Acknowledgements

This work was supported by the Natural Science Foundation of China [82172786], the National Cancer Center Climbing Fund of China [NCC201908B06], and the Natural Science Foundation of Heilongjiang Province [LH2021H077].

Appendix A. Supplementary data

Supplementary data related to this article can be found at https://doi.org/10.1016/j.ebiom.2023.104920.

References

1 Sung H, Ferlay J, Siegel RL, et al. Global cancer statistics 2020: GLOBOCAN estimates of incidence and mortality worldwide for 36 cancers in 185 countries. *CA Cancer J Clin*. 2021;71(3):209–249.
2 Wu HX, Pan YQ, He Y, et al. Clinical benefit of first-line programmed death-1 antibody plus chemotherapy in low programmed cell death ligand 1-expressing esophageal squamous cell carcinoma: a post hoc analysis of JUPITER-06 and meta-analysis. *J Clin Oncol*. 2023;41(9):1735–1746.
3 Patel MA, Kratz JD, Lubner SJ, Loconte NK, Uboha NV. Esophagogastric cancers: integrating immunotherapy therapy into current practice. *J Clin Oncol*. 2022;40(24):2751–2762.
4 Tang D, Kang R, Berghe TV, Vandenabeele P, Kroemer G. The molecular machinery of regulated cell death. *Cell Res*. 2019;29(5):347–364.
5 Overholtzer M, Mailleux AA, Mouneimne G, et al. A nonapoptotic cell death process, entosis, that occurs by cell-in-cell invasion. *Cell*. 2007;131(5):966–979.
6 Pasparakis M, Vandenabeele P. Necroptosis and its role in inflammation. *Nature*. 2015;517(7534):311–320.
7 Tsvetkov P, Coy S, Petrova B, et al. Copper induces cell death by targeting lipoylated TCA cycle proteins. *Science*. 2022;375(6586):1254–1261.
8 Song X, Zhu S, Xie Y, et al. JTC801 induces pH-dependent death specifically in cancer cells and slows growth of tumors in mice. *Gastroenterology*. 2018;154(5):1480–1493.
9 Holze C, Michaudel C, Mackowiak C, et al. Oxeiptosis, a ROS-induced caspase-independent apoptosis-like cell-death pathway. *Nat Immunol*. 2018;19(2):130–140.
10 Dixon SJ, Lemberg KM, Lamprecht MR, et al. Ferroptosis: an iron-dependent form of nonapoptotic cell death. *Cell*. 2012;149(5):1060–1072.
11 Chen X, He WT, Hu L, et al. Pyroptosis is driven by non-selective gasdermin-D pore and its morphology is different from MLKL channel-mediated necroptosis. *Cell Res*. 2016;26(9):1007–1020.

12 David KK, Andrabi SA, Dawson TM, Dawson VL. Parthanatos, a messenger of death. *Front Biosci (Landmark Ed)*. 2009;14(3):1116–1128.
13 Klionsky DJ. Autophagy: from phenomenology to molecular understanding in less than a decade. *Nat Rev Mol Cell Biol*. 2007;8(11):931–937.
14 Aits S, Jaattela M. Lysosomal cell death at a glance. *J Cell Sci*. 2013;126(Pt 9):1905–1912.
15 Gaziev AI, Fomenko LA, Sukhoruchkina LV, Kuzin AM. [Analysis of internucleotide breakages, repairable by polynucleotide ligase, in DNA irradiated by gamma-rays]. *Dokl Akad Nauk SSSR*. 1971;199(1):216–218.
16 Hanggi K, Ruffell B. Cell death, therapeutics, and the immune response in cancer. *Trends Cancer*. 2023;9(5):381–396.
17 Fu J, Li K, Zhang W, et al. Large-scale public data reuse to model immunotherapy response and resistance. *Genome Med*. 2020;12(1):21.
18 Nan Z, Dou Y, Chen A, et al. Identification and validation of a prognostic signature of autophagy, apoptosis and pyroptosis-related genes for head and neck squamous cell carcinoma: to imply therapeutic choices of HPV negative patients. *Front Immunol*. 2022;13:1100417.
19 Lu D, Liao J, Cheng H, et al. Construction and systematic evaluation of a machine learning-based cuproptosis-related lncRNA score signature to predict the response to immunotherapy in hepatocellular carcinoma. *Front Immunol*. 2023;14:1097075.
20 Chen Y, Tang L, Huang W, et al. Identification of a prognostic cuproptosis-related signature in hepatocellular carcinoma. *Biol Direct*. 2023;18(1):4.
21 Hu Y, Cai J, Ye M, et al. Development and validation of immunogenic cell death-related signature for predicting the prognosis and immune landscape of uveal melanoma. *Front Immunol*. 2022;13:1037128.
22 Li Q, Tang Y, Wang T, Zhu J, Zhou Y, Shi J. Novel immunogenic cell death-related risk signature to predict prognosis and immune microenvironment in lung adenocarcinoma. *J Cancer Res Clin Oncol*. 2023;149(1):307–323.
23 Liu Y, Wu L, Ao H, et al. Prognostic implications of autophagy-associated gene signatures in non-small cell lung cancer. *Aging (Albany NY)*. 2019;11(23):11440–11462.
24 Chen DS, Mellman I. Oncology meets immunology: the cancer-immunity cycle. *Immunity*. 2013;39(1):1–10.
25 Zhang Y, Chen H, Mo H, et al. Single-cell analyses reveal key immune cell subsets associated with response to PD-L1 blockade in triple-negative breast cancer. *Cancer Cell*. 2021;39(12):1578–15793.e8.
26 Cao K, Ling X, Jiang X, Ma J, Zhu J. Pan-cancer analysis of UBE2T with a focus on prognostic and immunological roles in lung adenocarcinoma. *Respir Res*. 2022;23(1):306.
27 Wang Y, Zhang D, Li Y, et al. Constructing a novel signature and predicting the immune landscape of colon cancer using N6-methylandenosine-related lncRNAs. *Front Genet*. 2023;14:906346.
28 Thomas AM, Fidelle M, Routy B, et al. Gut OncoMicrobiome Signatures (GOMS) as next-generation biomarkers for cancer immunotherapy. *Nat Rev Clin Oncol*. 2023;20(9):583–603.
29 Wang L, Chen X, Zhang H, et al. Comprehensive analysis of transient receptor potential channels-related signature for prognosis, tumor immune microenvironment, and treatment response of colorectal cancer. *Front Immunol*. 2022;13:1014834.
30 Necchi A, Joseph RW, Loriot Y, et al. Atezolizumab in platinum-treated locally advanced or metastatic urothelial carcinoma: post-progression outcomes from the phase II IMvigor210 study. *Ann Oncol*. 2017;28(12):3044–3050.
31 Hugo W, Zaretsky JM, Sun L, et al. Genomic and transcriptomic features of response to anti-PD-1 therapy in metastatic melanoma. *Cell*. 2016;165(1):35–44.
32 Ascierto ML, McMiller TL, Berger AE, et al. The intratumoral balance between metabolic and immunologic gene expression is associated with anti-PD-1 response in patients with renal cell carcinoma. *Cancer Immunol Res*. 2016;4(9):726–733.
33 van den Ende T, de Clercq NC, van Berge Henegouwen MI, et al. Neoadjuvant chemoradiotherapy combined with atezolizumab for resectable esophageal adenocarcinoma: a single-arm phase II feasibility trial (PERFECT). *Clin Cancer Res*. 2021;27(12):3351–3359.
34 Li LX, Zhang X, Zhang H, et al. Single-cell and CellChat resolution identifies collecting duct cell subsets and their communications with adjacent cells in PKD kidneys. *Cells*. 2022;12(1).
35 Zheng Y, Chen Z, Han Y, et al. Immune suppressive landscape in the human esophageal squamous cell carcinoma microenvironment. *Nat Commun*. 2020;11(1):6268.
36 Bischoff P, Trinks A, Obermayer B, et al. Single-cell RNA sequencing reveals distinct tumor microenvironmental patterns in lung adenocarcinoma. *Oncogene*. 2021;40(50):6748–6758.
37 Jin S, Guerrero-Juarez CF, Zhang L, et al. Inference and analysis of cell-cell communication using CellChat. *Nat Commun*. 2021;12(1):1088.
38 Tang D, Chen X, Kang R, Kroemer G. Ferroptosis: molecular mechanisms and health implications. *Cell Res*. 2021;31(2):107–125.
39 Levine B, Kroemer G. Biological functions of autophagy genes: a disease perspective. *Cell*. 2019;176(1-2):11–42.
40 Tang D, Chen X, Kroemer G. Cuproptosis: a copper-triggered modality of mitochondrial cell death. *Cell Res*. 2022;32(5):417–418.
41 Robinson N, Ganesan R, Hegedus C, Kovacs K, Kufer TA, Virag L. Programmed necrotic cell death of macrophages: focus on pyroptosis, necroptosis, and parthanatos. *Redox Biol*. 2019;26:101239.
42 Tang R, Xu J, Zhang B, et al. Ferroptosis, necroptosis, and pyroptosis in anticancer immunity. *J Hematol Oncol*. 2020;13(1):110.
43 Venables WN, Ripley BD, Venables WN. *Modern applied statistics with S*. 4th ed. New York: Springer; 2002:495.
44 Aho K, Derryberry D, Peterson T. Model selection for ecologists: the worldviews of AIC and BIC. *Ecology*. 2014;95(3):631–636.
45 Petitprez F, Levy S, Sun CM, et al. The murine Microenvironment Cell Population counter method to estimate abundance of tissue-infiltrating immune and stromal cell populations in murine samples using gene expression. *Genome Med*. 2020;12(1):86.
46 Li B, Severson E, Pignon JC, et al. Comprehensive analyses of tumor immunity: implications for cancer immunotherapy. *Genome Biol*. 2016;17(1):174.
47 Aran D, Hu Z, Butte AJ. xCell: digitally portraying the tissue cellular heterogeneity landscape. *Genome Biol*. 2017;18(1):220.
48 Racle J, de Jonge K, Baumgaertner P, Speiser DE, Gfeller D. Simultaneous enumeration of cancer and immune cell types from bulk tumor gene expression data. *Elife*. 2017;6.
49 Finotello F, Mayer C, Plattner C, et al. Molecular and pharmacological modulators of the tumor immune contexture revealed by deconvolution of RNA-seq data. *Genome Med*. 2019;11(1):34.
50 Newman AM, Liu CL, Green MR, et al. Robust enumeration of cell subsets from tissue expression profiles. *Nat Methods*. 2015;12(5):453–457.
51 Yoshihara K, Shahmoradgoli M, Martinez E, et al. Inferring tumour purity and stromal and immune cell admixture from expression data. *Nat Commun*. 2013;4:2612.
52 Subramanian A, Tamayo P, Mootha VK, et al. Gene set enrichment analysis: a knowledge-based approach for interpreting genome-wide expression profiles. *Proc Natl Acad Sci U S A*. 2005;102(43):15545–15550.
53 Dinh HQ, Pan F, Wang G, et al. Integrated single-cell transcriptome analysis reveals heterogeneity of esophageal squamous cell carcinoma microenvironment. *Nat Commun*. 2021;12(1):7335.
54 Zheng L, Qin S, Si W, et al. Pan-cancer single-cell landscape of tumor-infiltrating T cells. *Science*. 2021;374(6574):abe6474.
55 Qiu X, Mao Q, Tang Y, et al. Reversed graph embedding resolves complex single-cell trajectories. *Nat Methods*. 2017;14(10):979–982.
56 Zhu J, Ao H, Liu M, Cao K, Ma J. UBE2T promotes autophagy via the p53/AMPK/mTOR signaling pathway in lung adenocarcinoma. *J Transl Med*. 2021;19(1):374.
57 Wang X, Liu Y, Leng X, et al. UBE2T contributes to the prognosis of esophageal squamous cell carcinoma. *Pathol Oncol Res*. 2021;27:632531.
58 Heagerty PJ, Lumley T, Pepe MS. Time-dependent ROC curves for censored survival data and a diagnostic marker. *Biometrics*. 2000;56(2):337–344.
59 Fausett SR, Sandjak A, Billard B, Braendle C. Higher-order epistasis shapes natural variation in germ stem cell niche activity. *Nat Commun*. 2023;14(1):2824.
60 Thorsson V, Gibbs DL, Brown SD, et al. The immune landscape of cancer. *Immunity*. 2019;51(2):411–412.
61 Casares N, Pequignot MO, Tesniere A, et al. Caspase-dependent immunogenicity of doxorubicin-induced tumor cell death. *J Exp Med*. 2005;202(12):1691–1701.

62 Zhang Z, Chen C, Fang Y, et al. Development of a prognostic signature for esophageal cancer based on nine immune related genes. *BMC Cancer*. 2021;21(1):113.
63 Durgan J, Tseng YY, Hamann JC, et al. Mitosis can drive cell cannibalism through entosis. *Elife*. 2017;6.
64 Lu T, Xu R, Li Q, et al. Systematic profiling of ferroptosis gene signatures predicts prognostic factors in esophageal squamous cell carcinoma. *Mol Ther Oncolytics*. 2021;21:134–143.
65 Shi X, Li Y, Pan S, et al. Identification and validation of an autophagy-related gene signature for predicting prognosis in patients with esophageal squamous cell carcinoma. *Sci Rep*. 2022;12(1):1960.
66 Cai W, Li Y, Huang B, Hu C. Esophageal cancer lymph node metastasis-associated gene signature optimizes overall survival prediction of esophageal cancer. *J Cell Biochem*. 2019;120(1):592–600.
67 Qu J, Shen C, Qin J, et al. The MR radiomic signature can predict preoperative lymph node metastasis in patients with esophageal cancer. *Eur Radiol*. 2019;29(2):906–914.
68 Lu M, Li J, Fan X, Xie F, Fan J, Xiong Y. Novel immune-related ferroptosis signature in esophageal cancer: an informatics exploration of biological processes related to the TMEM161B-AS1/hsa-miR-27a-3p/GCH1 regulatory network. *Front Genet*. 2022;13:829384.
69 Zou Y, Xie J, Zheng S, et al. Leveraging diverse cell-death patterns to predict the prognosis and drug sensitivity of triple-negative breast cancer patients after surgery. *Int J Surg*. 2022;107:106936.
70 Gao Y, Zhang X, Li Y, et al. A novel pyroptosis-related signature predicts prognosis and indicates immunotherapy in oral squamous cell carcinoma. *J Cancer Res Clin Oncol*. 2023;149(13):12057–12070.
71 Li L, Sun F, Kong F, et al. Characterization of a cuproptosis-related signature to evaluate immune features and predict prognosis in colorectal cancer. *Front Oncol*. 2023;13:1083956.
72 Zhu J, Cao K, Zhao M, et al. Improvement of ACK1-targeted therapy efficacy in lung adenocarcinoma using chloroquine or bafilomycin A1. *Mol Med*. 2023;29(1):6.
73 Cao K, Liu M, Ma K, Jiang X, Ma J, Zhu J. Prediction of prognosis and immunotherapy response with a robust immune-related lncRNA pair signature in lung adenocarcinoma. *Cancer Immunol Immunother*. 2022;71(6):1295–1311.
74 Liu C, Lu Z, Yan J, et al. Construction of a prognostic signature associated with liver metastases for prognosis and immune response prediction in colorectal cancer. *Front Oncol*. 2023;13:1234045.
75 Binnewies M, Roberts EW, Kersten K, et al. Understanding the tumor immune microenvironment (TIME) for effective therapy. *Nat Med*. 2018;24(5):541–550.
76 Wen J, Fang S, Hu Y, et al. Impacts of neoadjuvant chemoradiotherapy on the immune landscape of esophageal squamous cell carcinoma. *eBioMedicine*. 2022;86:104371.
77 Trapnell C, Cacchiarelli D, Grimsby J, et al. The dynamics and regulators of cell fate decisions are revealed by pseudotemporal ordering of single cells. *Nat Biotechnol*. 2014;32(4):381–386.
78 Cao J, Huang YQ, Jiao S, Lan XB, Ge MH. Clinicopathological and prognostic significance of SHP2 and Hook1 expression in patients with thyroid carcinoma. *Hum Pathol*. 2018;81:105–112.
79 Nakade H, Migita K, Matsumoto S, et al. Overexpression of Cullin4A correlates with a poor prognosis and tumor progression in esophageal squamous cell carcinoma. *Int J Clin Oncol*. 2020;25(3):446–455.
80 Zhang L, Li L, Chen X, et al. Evodiamine inhibits ESCC by inducing M-phase cell-cycle arrest via CUL4A/p53/p21 axis and activating noxa-dependent intrinsic and DR4-dependent extrinsic apoptosis. *Phytomedicine*. 2023;108:154493.